

**PHOTOLUMINESCENCE CHARACTERIZATION
AND MORPHOLOGY CONTROL OF INORGANIC
PHOSPHOR PARTICLES**

TAKA AKI MINAMI

HIROSHIMA UNIVERSITY

MARCH 2009

PHOTOLUMINESCENCE CHARACTERIZATION
AND MORPHOLOGY CONTROL OF INORGANIC
PHOSPHOR PARTICLES

A Dissertation Submitted to
The Department of Chemical Engineering
Graduate School of Engineering
Hiroshima University

by

TAKA AKI MINAMI

In Partial Fulfillment of the Requirements
for the Degree of

Doctor of Engineering

Approved by

Professor Kikuo Okuyama
Advisor

March 2009

Abstract

The objective of this thesis is to investigate the photoluminescence characterization and morphologic control of inorganic phosphor particles. Both solid/dense and porous particles of europium-doped yttrium oxide ($\text{Y}_2\text{O}_3:\text{Eu}^{3+}$), and newly synthesized carbon-based boron oxynitride (BCNO) phosphors were selected as model materials. The major conclusions of this thesis can be summarized as follows.

Chapter 1 discusses the background, previous research, methods used to investigate photoluminescence phenomena, current state of the field, and problems associated with inorganic phosphors.

Chapter 2 describes the relationship between photoluminescence and both the particle and crystallite size of $\text{Y}_2\text{O}_3:\text{Eu}^{3+}$ fine particles. The crystallite and particle sizes played different roles in the control of the photoluminescence characteristics of the phosphors. The blue-shift of the charge transfer band in the excitation spectra was mostly due to the particle-size effect. In contrast, the decrease in the crystal symmetry ratio, which is the ratio of the C_2 to C_{3i} sub-lattice populations in the photoluminescence emission spectra, was primarily due to the effect of crystallite size.

Chapter 3 demonstrates the effect of porosity on the photoluminescence of $\text{Y}_2\text{O}_3:\text{Eu}^{3+}$ fine particles. The porous particles exhibited greater red-emission rendering properties than that of non-porous particles, based on the CIE chromaticity diagram. The photoluminescence intensity and quantum efficiency exhibited by the porous particles are greater than that of non-porous particles because the porous particles are hollow. Porous particles have unique photophysical properties, such as a 4-nm blue-shift in the charge-transfer and a lower symmetry ratio of 2.7, which were not exhibited by

the non-porous particles with a particle size of 757 nm and a crystallite size of approximately 30 nm. The properties of sub-micrometer porous particles were identical to those of non-porous particles, which have reduced particle and crystallite size compared with porous particles.

Chapter 4 presents a detailed chemical analysis and photoluminescence characterization of the BCNO phosphors. The resulting powder has high external quantum efficiency with a direct band-gap transition. The BCNO phosphors have these properties because the atomic distances of the BCNO are less than those of conventional BCN compounds, which have an indirect band-gap transition and low quantum efficiency. The smaller atomic distances of the BCNO result from the presence of oxygen atoms, which have higher electron affinity and smaller covalent-bond radii compared with boron, carbon and nitrogen.

A simple summary and comments regarding future investigations are provided in **Chapter 5**.

Contents

Abstract	I
Contents	III
1. Introduction	1
1.1 Background	1
1.2 Photoluminescence Phenomena	2
1.2.1 Principles of Photoluminescence Phenomena	2
1.2.2 Time-resolved Photoluminescence Analysis	5
1.3 Previous Research on Inorganic Phosphor Particles	14
1.3.1 Inorganic Phosphors	14
1.3.2 Preparation Methods	18
1.3.3 Photoluminescence Characterization	21
1.3.4 Control of Morphology	29
1.4 Objectives	31
1.5 Outline of the Thesis	31
References	33
2. Photoluminescence Properties of Submicrometer Phosphors with Different Crystallite/Particle Sizes	39
2.1 Introduction	39
2.2 Experimental Procedure	40
2.3 Results and Discussion	40
2.3.1 Morphology, Particle Size and Crystallinity Characterization	41
2.3.2 Excitation Spectrum Characterization	44
2.3.3 Emission Spectra Characterization	48
2.4 Summary	52
References	53

3. Photoluminescence Characteristics of Ordered Macroporous Eu-doped Yttrium Oxide Particles Prepared by Spray Pyrolysis	55
3.1 Introduction	55
3.2 Experimental Procedure	56
3.3 Results and Discussion	58
3.3.1 Morphology, Particle Size and Crystallinity Characterization	58
3.3.2 Photoluminescence Spectra	64
3.3.3 Color Rendering Properties	70
3.4 Summary	72
References	73
4. Chemical and Photoluminescence Analysis of New Carbon-based Boron Oxynitride Phosphor Particles	75
4.1 Introduction	75
4.2 Experimental Procedure	76
4.3 Results and Discussion	77
4.3.1 Chemical Analysis	77
4.3.2 Photoluminescence Characterization	81
4.4 Summary	85
References	86
5. Summary	89
5.1 Conclusions	89
5.2 Suggestions for Further Investigations	91
Acknowledgements	92
Appendix I: List of Figures.....	93
Appendix II: List of Tables.....	97
Appendix III: List of Publications.....	98

Chapter 1

Introduction

1.1 Background

Light is ubiquitous, and it is of great importance. For example, “Let there be light,” is a well-known sentence from the Bible. Amaterasu, a Japanese goddess, represents the sun. For living things, the sun is the source of both energy and light.

In addition, investigations of luminescent phenomena have made significant contributions to the evolution of scientific knowledge, and practical application of the results of these studies have improved our lives. The 2008 Nobel Prize for Chemistry was awarded for the discovery and development of green fluorescent protein (GFP). Applications of GFP have been developed, including its use in the development of induced pluripotent stem (iPS) cells, which could be an achievement that wins another Nobel Prize.

Regarding the development of electronic devices, the cathode ray tube (CRT) was invented by Karl F. Braun in 1897. Since then, novel displays such as liquid crystal displays (LCD), plasma display panels (PDP), field emission displays (FED), and organic and inorganic electroluminescence (EL), have been developed. These displays are critical components of instruments that serve important functions in our daily lives. In addition to these displays, luminescent devices have been invented, including fluorescent lamps, light-emitting diodes (LED), and laser diodes (LD). Inorganic phosphor particles play an important role in the development of these devices.

1.2 Photoluminescence Phenomena

1.2.1 Principles of Photoluminescence Phenomena

The development and improvement of these devices requires an understanding of basic luminescent phenomena. Luminescent phenomena occur due to interactions between atoms and photons. The many types of luminescent phenomena are classified by their excitation source, as follows: photoluminescence by photon (electromagnetic wave); cathode luminescence by electron beam; electroluminescence by electronic potential; chemiluminescence by chemical energy; bioluminescence by chemical energy from adenosine triphosphate (ATP); and, trioboluminescence by friction. The terms, fluorescence and photoluminescence, are synonymous. Generally, fluorescence is used in chemistry, while photoluminescence is used in physics. The applications of these phenomena are listed in Table 1.1.

The electronic absorption and emission spectra of a molecule/atom provide important information about the structure, energetics, and dynamics of the electronically excited state. The interaction between light and a molecule/atom depends on resonance. The oscillations of the first system are related to the oscillations of the second system. Strict requirements exist for the achievement of effective resonance: the systems must interact; and, the law of energy conservation must be satisfied:

$$\Delta E = h\nu \quad (1-1)$$

Here, ΔE is the energy gap between two electronic states of a molecule, h is Plank's constant, and ν is the frequency of the oscillation of the light wave. According to equation (1-1), the possible interactions between light and a molecule/atom depend on the energy gap of the oscillations that are possible for the electrons of the molecule/atom. (Turro, 1978)

Using equation (1-1), only the absorption and emission spectra of atoms come close to being "sharp lines," as shown in Fig.1.1(a). This sharpness exists because the electronic states of atoms can be accurately described by specification of the orbits of

Table 1.1 Luminescent Phenomena (Kobayashi, 2000)

Phenomena	Energy Source	Applications
Photoluminescence	Light/ Electromagnetic Wave	Fluorescent lamp, PDP
Cathode luminescence	Electron beam	CRT
Electroluminescence	Electronic potential	EL Display
	Carrier injection	LED, LD
X-ray luminescence	X-ray	Scintillator
Chemiluminescence	Chemical energy	Chemical laser
Bioluminescence	Adenosine triphosphate (ATP) / Luciferin/Luciferase	Firefly, Firefly squid,
	Ca ion/aequorin	Aequorea Victoria / Ca sensor
Triboluminescence	Friction	None developed to date
	Mechanical shock	
Thermoluminescence	Heat	Tungsten lamp

PDP = Plasma Display Panel, CRT = Cathode Ray Tube, EL = Electroluminescence,

LED = Light Emitting Diode, LD = Laser Diode.

their valence electrons. In a molecule, an electronic transition is not as “pure” as it is in an atom. The motion of nuclei relative to one another, e.g., vibrations, rotations and collisions, must be taken into account. A molecular electronic transition does not correspond to a well-defined quantum of energy because both the initial and final states may consist of an ensemble of different nuclear shapes. As a result, both the absorption and emission spectra of a molecule may involve the transitions shown in Fig.1.1(b).

Given the molecular transition mechanism, the shape of the excitation spectrum is similar to that of the absorption spectrum in Fig.1.2. Absorption spectra cannot be obtained for solid samples, because light is not transmitted between atoms in the solid state. When the material exhibits photoluminescence, the excitation spectrum, which is measured at a fixed wavelength with variable excitation, is used instead of the absorption spectrum. The mechanism responsible for the excitation spectrum is the same as that which results in the absorption spectrum.

1.2.2 Time-resolved Photoluminescence Analysis

Measurement of absorbance and photoluminescence reveals the energy levels of the atoms/molecules. Time-resolved measurements allow for determination of the energy-transfer rate of each energy level. As an example, we will describe one method by which the rate constant can be measured (O'Conner et al., 1985). When molecule [M] is excited to [M*], then [M*] loses the energy to [M]. The decay of the excited state is expressed using three rate constants: photoluminescence (k_p), non-radiative transition (k_{nr}), and energy transfer (k_e). The concentration of the excited species is represented as [M*]. The decay of the excited state is represented schematically in Fig.1.3:

$$-d[M^*] / dt = (k_p+k_{nr}+k_e)[M^*] \quad (1-2)$$

$$\tau = 1 / (k_p+k_{nr}+k_e) \quad (1-3)$$

Here, τ is the photoluminescence lifetime, which expressed by the reciprocal of the sum of the three rate constants. Time-resolved photoluminescence is a very useful tool for the investigation of a particular system. Photoluminescence lifetime is the expression used to describe photoluminescence decay.

$$F(t) = \int_0^t L(t) e^{-(t-t')} dt, \quad F(t) = \sum A_i e^{-(t/\tau_i)} \quad (1-4)$$

Here, t is time, $F(t)$ is photoluminescence decay, $L(t)$ is the pump pulse used for excitation, A_i is the pre-exponential factor for each τ_i , and τ_i is i -th photoluminescence lifetime. Examples of photoluminescence lifetimes (τ) for various compounds are shown in Table 1.2. Because τ depends on both the specific molecule and the environment (solvent, degassed and undegassed), τ describes the molecular environment.

Non-exponential photoluminescence decay is common in real systems, especially in heterogeneous systems, such as interfaces, polymers, biological systems, etc. Time-correlated single photon counting (TC-SPC) has enabled reliable measurement of

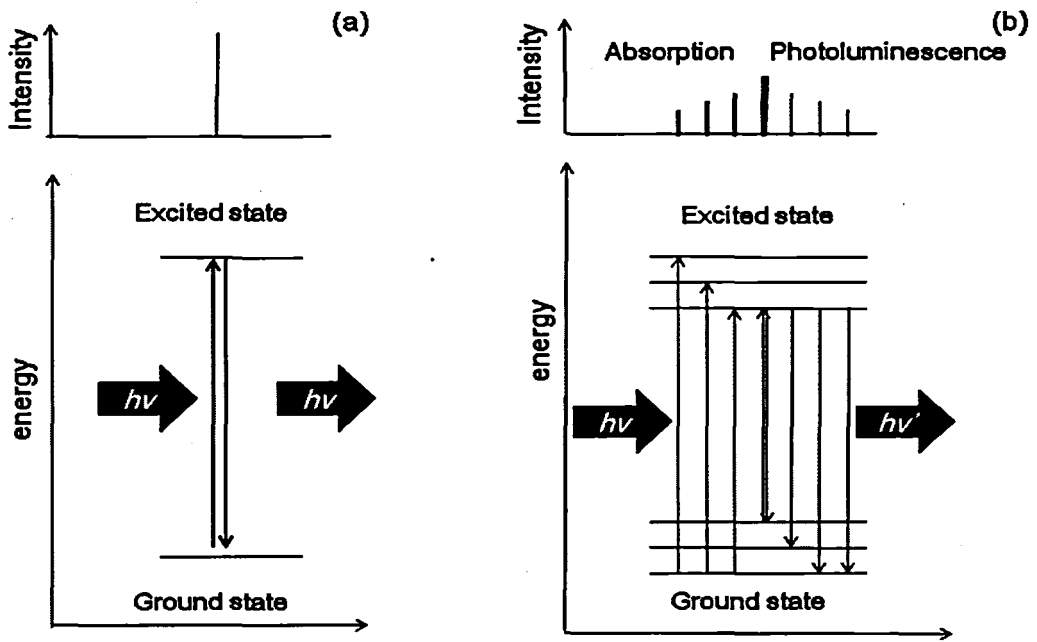


Fig.1.1 Absorption and photoluminescent mechanism. (a) atom, and (b) molecule

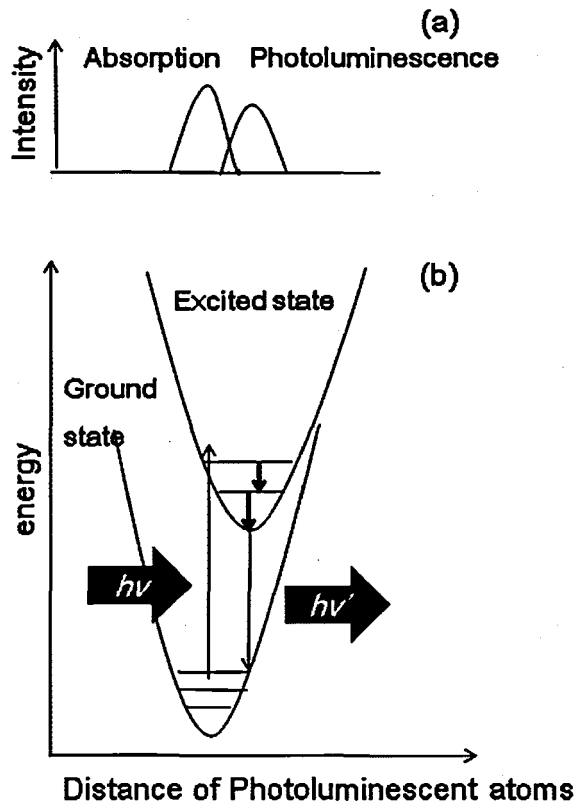


Fig.1.2 Relation between (a) absorption and photoluminescence spectra, and (b) energy diagram of the ground and excited bands

photoluminescence lifetime. However, because the TC-SPC method is based on statistical principles, it requires a longer data acquisition time than other techniques (O'Conner et al., 1985).

Consequently, it is extremely difficult to obtain non-exponential decay curves using the TC-SPC method for a sample that suffers from significant bleaching during analysis. Therefore, a reliable and fast method other than the TC-SPC method is required. For example, the intrinsic disadvantage of the TC-SPC technique can be overcome by use of a streak camera.

Currently, several methods for the measurement of photoluminescence lifetime are available (Lakowicz, 1991). Two types of instrumentation that both provide high-quality photoluminescence decay curves and determination of lifetime are discussed as examples of how to analyze the photoluminescence mechanism presented in Fig.1.4 and Table 1.3.

For example, a solid-state sample of tetra phenyl porphyrin (TPP) powder was measured using either a streak camera or the TC-SPC method. Figure 1.4 shows a typical three-exponential decay curve, and the photoluminescence lifetimes are shown in Table 1.3. These methods yield the same range of photoluminescence lifetimes, but differ in time-division and method. Therefore, both methods yield high-quality measurements of photoluminescence lifetime. In solution, this sample exhibits one exponential decay curve. For the solid state in air, oxygen molecules collide with the TPP surface, and energy transfer occurs from the excited state of TPP to the ground state of the oxygen molecule. Thus, TPP surface in the solid state shows the shortest photoluminescence lifetime. In the solid crystallite, oxygen does not act as a quenching agent, resulting in the longest photoluminescence lifetime. The photoluminescence lifetime of the crystallite boundary is intermediate to that of the solid state in air and the solid crystallite. Since chemical species has three kinds of environments, crystallite inside, crystallite surface, and particle surface which is attacked by oxygen, then it exhibits three different photoluminescence lifetimes. Similar phenomenon is observed in photoluminescence character for inorganic phosphors. This will be discussed in chapter 2.

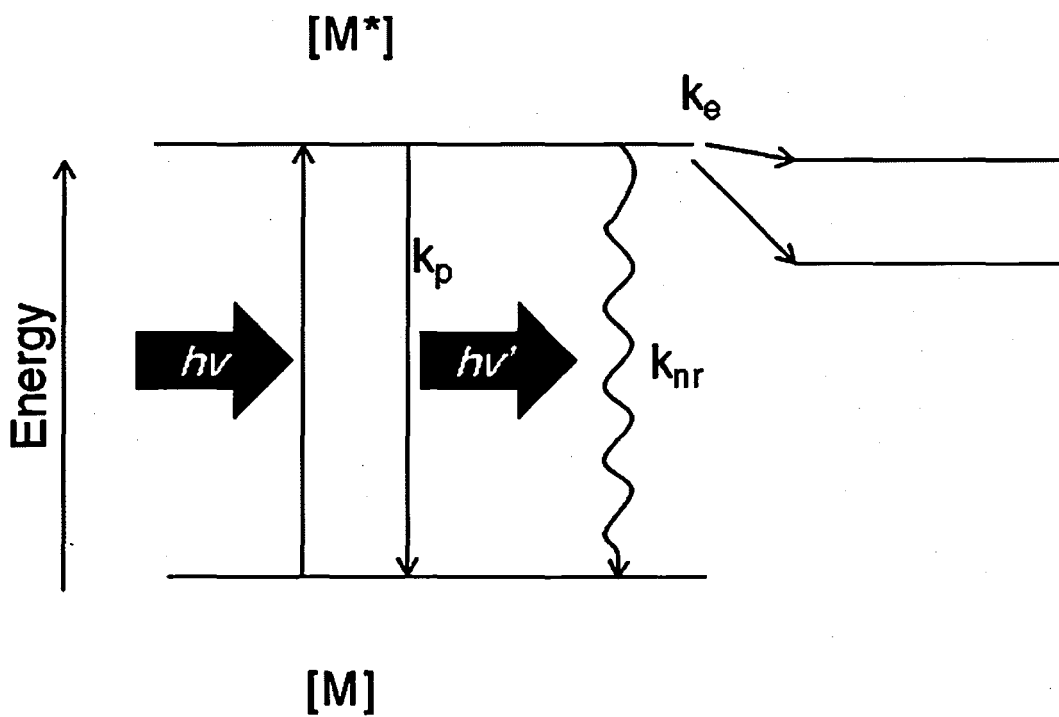


Fig.1.3 Schematic representation of the energy diagram of the species, M

Table 1.2 Photoluminescence lifetimes of various materials in liquid ($1 \times 10^{-5} \text{M}$) measured using a streak camera and the TC-SPC technique. (Minami et al., 1990)

Sample	Solvent	Streak camera	TC-SPC	Literature
		τ (ns)	τ (ns)	τ (ns)
Erythrosin	H ₂ O	0.092±0.001	0.085±0.004	0.081 (Rogers et al., 1983) 0.115 (Fleming et al., 1977)
	EtOH ^d	0.624±0.007	0.64±0.01	0.565 (Fleming et al., 1977)
Rhodamine B	H ₂ O	1.29±0.03	1.41±0.03	1.97 (Ware et al., 1983)
	EtOH ^d	2.72±0.09	2.80±0.04	2.85 (Lampert et al., 1983)
ZnTPP	Acetone ^u	1.96±0.06	2.01±0.04	1.9 (Blondeel et al., 1984)
Acridine Orange	EtOH ^d	3.49±0.12	3.63±0.05	2.8 (Stich et al., 1979)
TPP	Benzene ^d	12.99±0.20	12.75±0.15	13.6 ^d (in Methylcyclohexane) (Harriman et al., 1980)

The symbols ^d and ^u indicate degassed and undegassed solutions, respectively. TPP = tetra phenyl porphyrin.

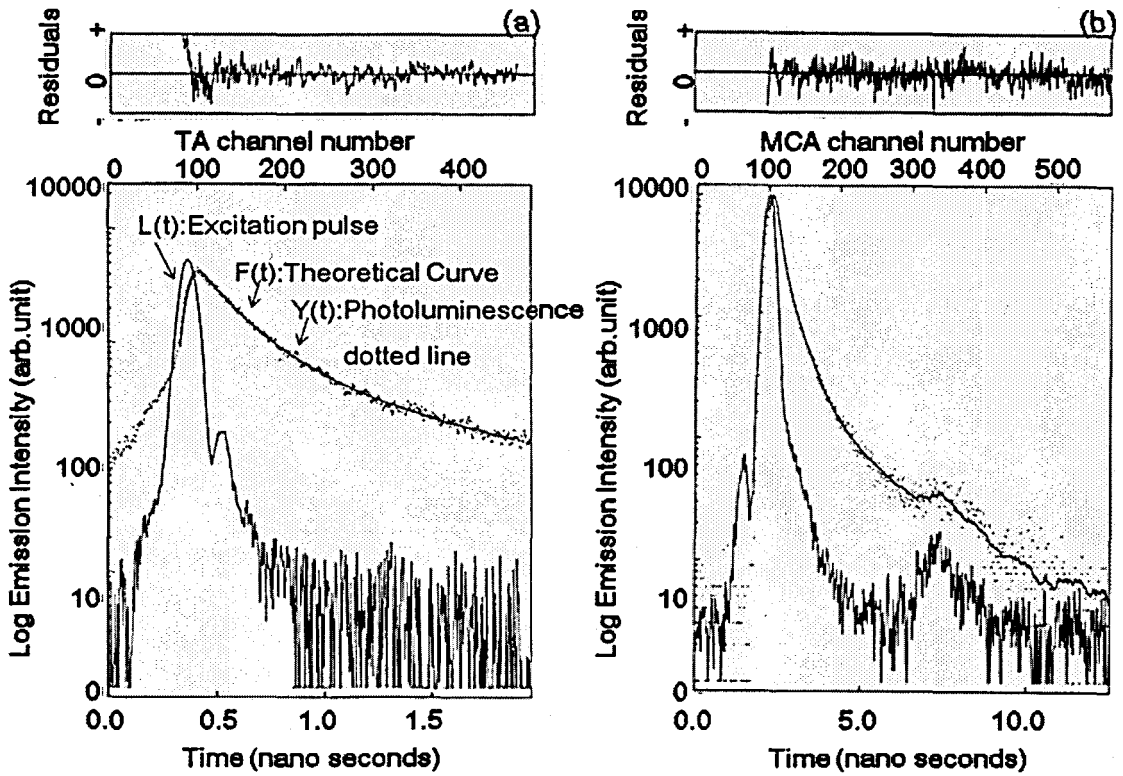


Fig.1.4 Photoluminescent decay curves of tetra phenyl porphyrin particles on a glass slide (a) observation using the streak camera method (b) observation using the TC-SPC method (Minami et al.,1990)

Table 1.3 Photoluminescence lifetimes of TPP deposit (Minami et al., 1990)

Condition	Photoluminescence lifetime* τ (ns)	Method
Aerated	0.08±0.01 (36.1)	TC-SPC
	0.29±0.02 (61.1)	
	1.36±0.46 (2.9)	
Aerated	0.102±0.005(32.2)	Streak
	0.253±0.007(50.0)	
	1.050±0.114(17.8)	

*The values in parentheses are the relative pre-exponential factors

A second example is TPP associated with quinone in solution (Osuka et al., 1987). Because quinone has high electron affinity, excited electrons transfer energy to quinone, and luminescence is quenched. TPP associated with para-substituted quinone has a luminescence lifetime that differs from TPP with meta-substituted quinone, due to the steric hindrance of the meta-substituted compound. A more detailed analysis of the energy-transfer mechanism requires an artificial photosynthesis system. These methods are now common in photoluminescence research, and these instruments are commercially available (Yokoyama et al., 1992).

1.3 Previous Research on Inorganic Phosphor Particles

1.3.1 Inorganic Phosphors

Phosphor is the term used for a material that exhibits luminescence, including luminescent powders and thin-film materials. Inorganic phosphors are the most common luminescent material used in fluorescent lamps. Solid-state lasers, optical amplifiers in fiber optics, rare-earth elements, and lanthanides, are widely used to activate luminescent and photonic materials. Generally, a phosphor is made by addition of a luminescent activator to a host crystal. Take, for example, $Y_2O_3:Eu^{3+}$. The compound on the left-hand side of the colon (in this case, Y_2O_3) represents the host crystal, while the compound to the right of the colon (in this example, Eu^{3+}) represents the luminescent ion, which is added in a trace amount to the host crystal. Fluorescent lamps use phosphors such as $Ca_2(PO_4)_2 \cdot Ca(F,Cl)_2:Sb^{3+}$, Mn^{2+} , $BaMgAl_{10}O_{17}:Eu^{2+}$ (blue), $LaPO_4:Tb^{3+}$ (green), and $Y_2O_3:Eu^{3+}$ (red). In addition, PDP use phosphors such as $BaMgAl_{10}O_{17}:Eu^{2+}$ (blue), $Zn_2SiO_4:Mn^{2+}$ (green), and $YBO_3:Eu^{3+}$ (red). Conventional CRT use $ZnS:Ag$ (blue), $ZnS:Cu, Au, Al$ (green) and $Y_2O_2S:Eu^{3+}$ (red). The most common inorganic phosphors are shown in Table 1.4. (Kobayashi, 2000)

Rare earth elements are included specific mineral resources and specific geological area, on the contrary typical metal elements are spread out on earth for geologically.

Rare earths do not mean rare in the earth, but they are still expensive to get, because they have difficulties to extract from the source minerals, which have low contents of rare earth, and they are similar physical property such as solubility, melting point and so on. If we can use phosphor, which made by light elements and easier synthesis condition, it is very useful phosphor for industry.

$Y_2O_3:Eu^{3+}$ has a body-centered cubic structure shown in Fig.1.5. Eu is commonly about 6 % substituted Y. Since the coordination number of Y is 6 for oxygen, two oxygen vacancies are in one unit lattice. Y_2O_3 has two kinds of sub-lattice, C_2 and C_3 ; according to symmetry theory. They have different photophysical properties, and it will be discussed in chapter 2 and 3.

Table 1.4 Luminescence Phenomena and Inorganic Phosphors (Kobayashi, 2000)

Phenomena	Energy Source	Material Example	Applications
Photoluminescence	Light/ Electromagnetic Wave	Ca ₂ (PO ₄) ₂ ·Ca(F,Cl) ₂ : Sb ³⁺ , Mn ²⁺ , BaMgAl ₁₀ O ₁₇ :Eu ²⁺ (blue), LaPO ₄ :Tb ³⁺ (green), Y ₂ O ₃ :Eu ³⁺ (red)	Fluorescent lamp, PDP
Cathode luminescence	Electron beam	ZnS:Ag (blue)	Color CRT
		ZnS:Cu, Au,Al (green)	
		Y ₂ O ₂ S:Eu ³⁺ (red).	
Electroluminescence	Electronic potential	ZnS:Mn ²⁺ (orange)	EL Display
	Carrier injection	GaP:N (green) InGaAsP(1.3 μm, 1.5 μm)	LED LD

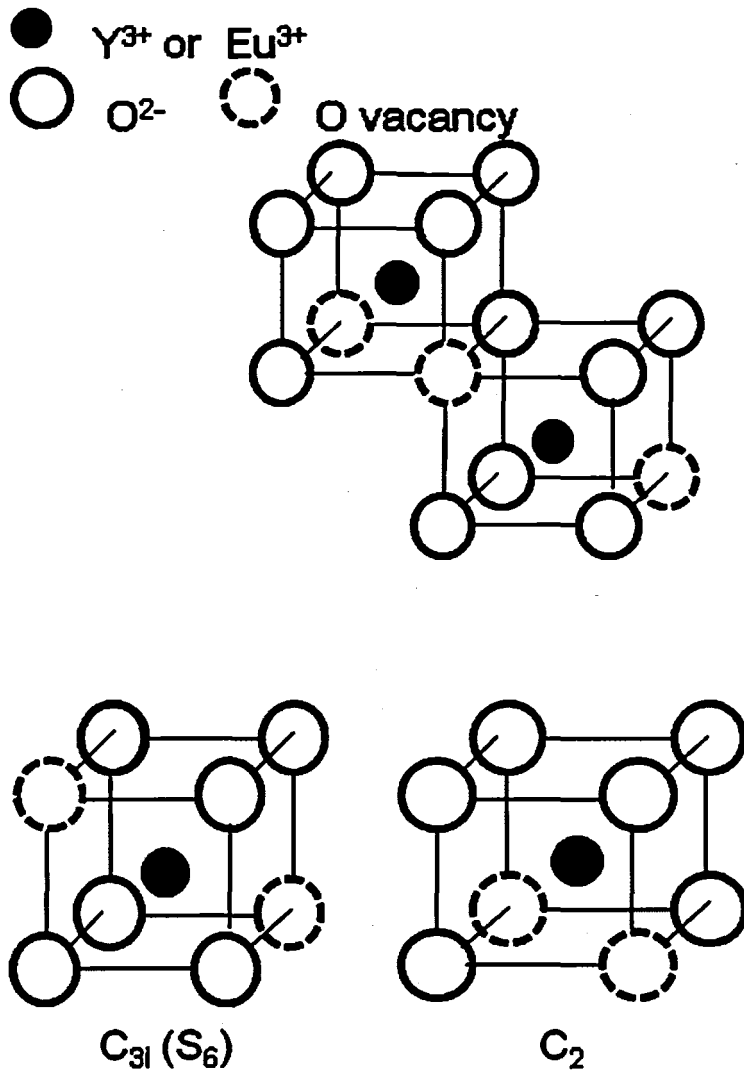


Fig.1.5 Schematic diagram of $Y_2O_3:Eu^{3+}$ lattice and its sub-lattices

Another useful inorganic phosphor is carbon-based boron oxynitride (BCNO). This compound is analogous of compound semiconductor, which has specific character. BCNO compound is designed based on graphite. Adding B and N elements to graphite, its character is changed to semiconductor and PL emission property. BCN has low efficiency of PL emission, adding O elements to make BCNO phosphor, it has high efficiency of PL emission.

We propose the use of BCNO compounds because these compounds are semiconductors, emit at a variety of wavelengths, and exhibit high-intensity luminescence. Additional studies of the PL mechanism will continue to produce improved luminescent phosphors.

1.3.2 Preparation Methods

To extend the use of phosphors to high-resolution and rendering applications, fine spherical phosphor particles with uniform composition and good surface properties are highly desirable. A variety of methods have been applied to the preparation of phosphors, as follows: hydrothermal (Wan et al., 2005), sol-gel (Zhang et al., 2002), copolymer micro-gel methods (Martinez-Rubio et al., 2001); precipitation (Jing et al., 1999; Silver et al., 2001); bi-continuous cubic phase processes (Chien, 2006); combustion (Kottaisamy et al., 1996); and, spray pyrolysis (Kang et al., 1999; Kang et al., 2000; Hong et al., 2003; Lenggono et al., 2003). Among these methods, the spray pyrolysis method shows promise, as it is an inexpensive, simple, rapid, and continuous process that can be used in the fabrication of diverse materials, including phosphors, with controllable size and composition (Xia et al., 2002). Particles prepared using the conventional spray pyrolysis (CSP) method is spherical with highly uniform size and composition. In addition, they are resistant to agglomeration because they are synthesized via micro-scale reactions that proceed within a single droplet. Submicrometer-to-micrometer sized particles are typically produced via the CSP method based on the one-droplet-to-one-particle assumption (ODOP) (Wang et al., 2007).

Many investigators have used additional treatments to improve PL intensity, such as addition of additives and flux materials to the precursors (Kang et al., 1999; Hong et al., 2003; Jung et al., 2005). The present study used the CSP method, which is shown schematically in Fig.1.6, (Wang et al., 2007), to prepare solid and porous $Y_2O_3:Eu^{3+}$ particles without additional treatments. This method can realize independent control of crystallite size and particle size. The crystallite size is controlled by the prepared temperature and the particle size is controlled by the precursor concentration.

In addition, a facile liquid process was used for the preparation of a BCNO phosphor. The BCNO phosphors were synthesized from the following precursors: boric acid (H_3BO_3), as the boron source; urea ($(NH_2)_2CO$), as the nitrogen source; and, polyethylene glycol (PEG), $(H(EG)_nOH$, with $M_w = 20,000$ and $EG = OCH_2CH_2$), as

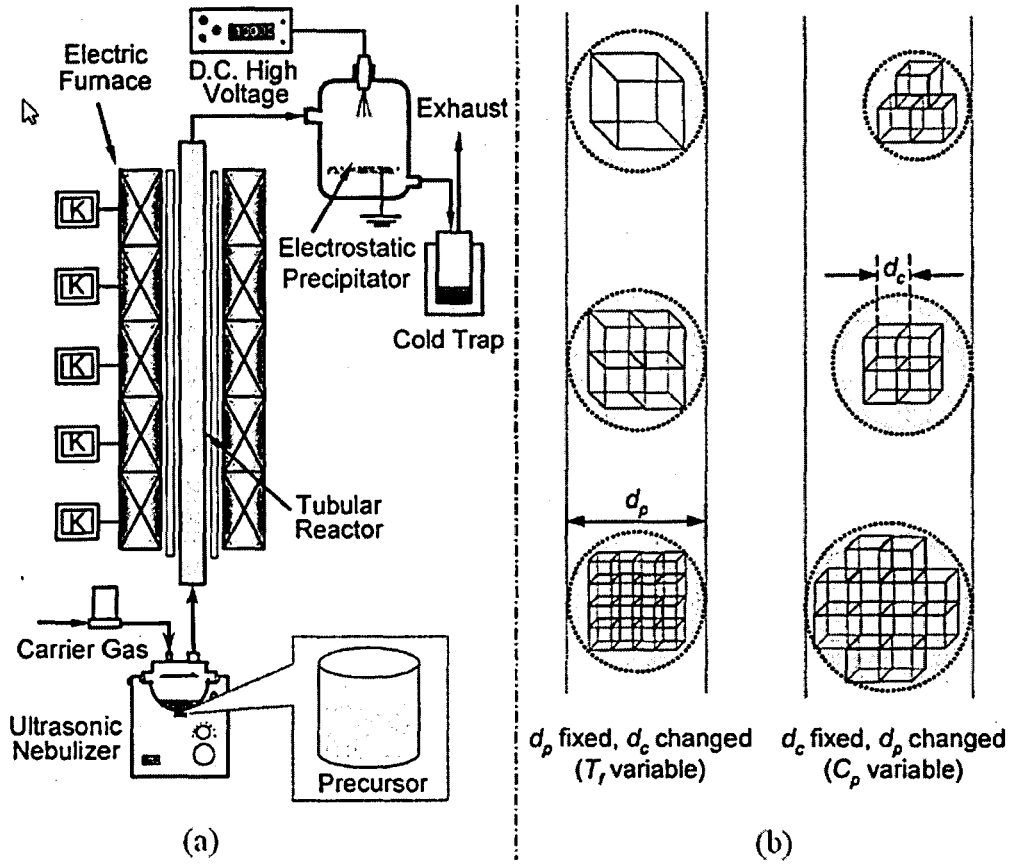


Fig.1.6 Schematic diagram of the experimental setup and procedures (Wang et al., 2007)

the carbon source. The precursors were mixed in pure water and the resulting solution was heated at 700-900 °C for 30-60 min to obtain BCNO particles. The detailed explanations were described in the previous paper (Ogi et al., 2008).

1.3.3 Photoluminescence Characterization

A schematic representation of the fluorescent mechanism of a rare-earth-doped Y_2O_3 inorganic phosphor using a coordinate model is shown in Fig.1.7. Fig. 1.7(a) shows the radiation transition, and the observed photoluminescence. Fig.1.7 (b) shows the non-radiation transition; no photoluminescence was observed.

The mechanism of the photoluminescence of the $Y_2O_3:Eu^{3+}$ phosphor can be explained as follows: (Liu et al., 2005)

- 1) Excitation of the host crystal (Y_2O_3) absorbs light energy ($h\nu$) in the Y-O bonding orbital.
- 2) The absorbed energy is transferred to the activator (Eu^{3+}).
- 3) The energy absorbed by Eu^{3+} promotes the transition from the ground state to the excited state.
- 4) The excited state loses energy as heat and lattice vibration, and returns to the bottom of the excited state curve.
- 5) In the case of $Y_2O_3:Eu^{3+}$, excited Eu^{3+} and O^{2-} form a metastable state, which is called the charge-transfer (CT) state. This metastable state then loses energy as light ($h\nu'$) from the bottom of the excited state to the ground state.

Because electronic motion is much faster than nuclear motion, electronic transitions are facilitated when the nuclear structures of the initial and final states are most similar. In Fig.1.7, both excitation and emission of light (electronic transitions) are vertical, consistent with the Frank-Condon principle. Fig. 1.7(b) shows a radiation-less transition. In this system, the coordination difference between the ground and excited states is large. The bottom of the excited state curve diverges from the ground state curve, and the excess energy is lost as heat resulting from lattice vibration.

In the case of the transition metal, Mn^{2+} , $Zn_2SiO_4:Mn^{2+}$ exhibits green luminescence and $MgSiO_3:Mn^{2+}$ shows red luminescence. The difference in luminescence occurs because

of the disparate crystal field splitting of the 3d orbital of Mn^{2+} . However, for rare earth elements, the wavelength of luminescence is not entirely dependent on the crystal field. The electron configuration of a trivalent rare earth element is $[\text{Xe}]4f^x5s^25p^6$; therefore, the 4f orbital is shielded by the outer shell, $5s^25p^6$.

In crystals, magnetic hyperfine splitting of Eu^{3+} is absent in both the ${}^7\text{F}_0$ ground state and the metastable ${}^5\text{D}_0$ excited state. Nuclear electric quadrupole interactions split the $J=0$ crystal field singlet into three hyperfine levels ($m=\pm 1/2, \pm 3/2, \pm 5/2$) that are separated by 10-100 MHz.

These applications capitalize on the unique properties of the 4f electrons that have localized states and exhibit both weak coupling to ligand electrons and lattice vibrations. Thus, the 4f spectroscopic properties, including the energy-level structure and the dynamics of the electronic transitions of rare earth ions in solids, largely define the optical properties of a rare-earth-activated device. With energy levels more than $30,000 \text{ cm}^{-1}$ above the ground states of the $4f^N$ configurations, there are 5d, 6s, 6p orbitals in the rare earth ion electronic structure. The 5d states are less localized, but have stronger coupling g-lattice vibrations. Because the inter-configuration $4f^N$ -to- $4f^{N-1}5d$ transitions are parity-allowed in the rare earth ions, they have intensities up to 10,000-fold stronger than the strongest $4f^N$ -to- $4f^N$ transitions. Due to these electronic properties, $4f^N$ -to- $4f^{N-1}5d$ transitions have become increasingly important in recent years for applications in fast scintillators and ultraviolet laser sources. A unique spectroscopic property of the solid-state rare earth elements is that the electronic energy level structure is established primarily using the quantum theory of atomic spectroscopy. Therefore, all collective solid-state effects can be viewed as a perturbation known as the crystal-field interaction. This simple approximation works very well for rare earth ions in a $4f^N$ configuration, in which the electrons in the partially occupied 4f shell are shielded by the electrons in the 5s and 5p shells from ligand interaction and, therefore, participate only minimally in chemical bond formation.

When a 4f electron is excited into a 5d orbital that extends beyond the 5s and 5p orbitals, the spectroscopic properties of the rare earth ions in an electronic configuration, such as $4f^{N-1}5d$, are more strongly influenced by the lattice. Therefore, the electronic

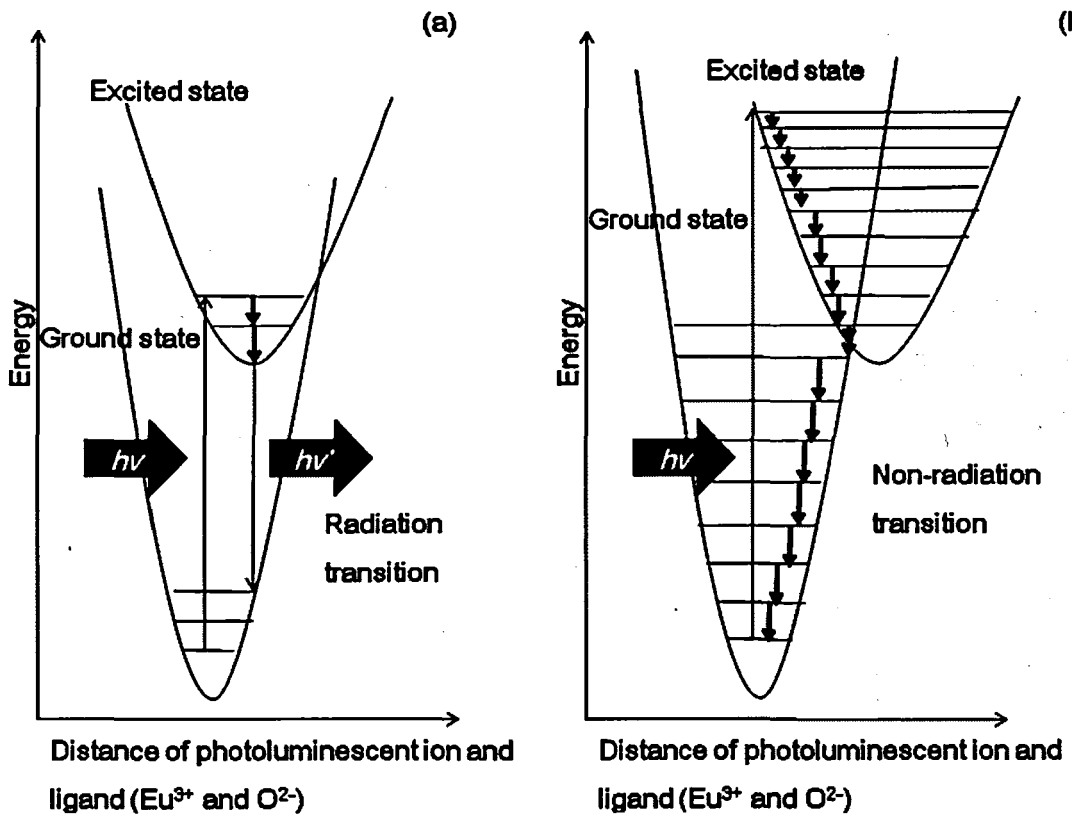


Fig.1.7 Schematic representation of (a) photoluminescent (radiation) and (b) non-radiation mechanisms.

transitions between the $4f^N$ and $4f^{N-1}5d$ states, through either absorption or emission of photons, are expected to exhibit characteristics that are very different from transitions within the $4f^N$ configuration. A modification of the crystal-field theory is necessary for modeling stronger ion-lattice interactions in the analysis of both energy-level splitting and excited-state dynamics.

The electronic configuration of the Eu ground state is $4f^6, 7F^0$. Both the energy levels of the $4f^N$ configurations and the binding energies are expressed relative to the host band. Charge-transfer bands are often observed in rare-earth materials. These bands are associated with excitation of a ligand electron into a 4f orbital. For some ions, especially Eu^{3+} , the charge transfer bands in many host crystals are located at energies less than the $4f^{n-1}5d$ states. For these transitions, the vibronic coupling in the excited state is very large and the transitions are completely dominated by the vibronic coupling. The excited state has one more 4f electron and a hole in the ligand orbitals. van Pieterse et al. (2000) extensively measured charge-transfer absorption and emission. The results shown in Table 1.5 demonstrate that the peaks of the CT band are dependent on the host crystal. Investigations of the CT band for the $\text{Y}_2\text{O}_3:\text{Eu}^{3+}$ phosphor particle will be discussed in Chapters 2 and 3.

Another inorganic phosphor, carbon-based boron oxynitride (BCNO) has been proposed as a novel inorganic phosphor. This phosphor is analogous to compound semiconductors, such as GaP, which is an extremely useful III-V compound semiconductor with an indirect band-gap. BCNO is a derivative of both boron nitride (hexagonal BN(h-BN)) and boron carbon nitride (BCN). BN is an insulator, but BCN is a semiconductor. Their original structure is hexagonal carbon base framework, such as graphite, which is a conductor since its conduction band and valence band are overlapped with 0.04 eV. The difference in the conductive properties of BN and BCN exists because of the difference in the band-gap. The band-gap of BN is greater than 3.8 eV (326 nm), while that of BCN depends on impurities. These photophysical characters and their structures are shown in Fig. 1.8. BCNO compounds are less expensive than Si compounds. Therefore, BCNO compounds have a potential to become the most widely used light-emitting semiconductor material of the future.

The PL properties of BN and BCN are shown in Table 1.6. Because BCN compounds are a mixture of B/C/N atoms, the PL wavelength of a BCN compound varies with its components. Studies of the BCNO phosphor will be discussed in Chapter 4.

Table 1.5 Position of the Eu^{3+} charge-transfer band of the ${}^5\text{D}_0 \rightarrow {}^7\text{F}_j$ photoluminescence after excitation in the charge-transfer band. (van Pieterse et al., 2000)

Host crystal	CT Band (nm)
Y_2O_3	250
$\text{Y}_2\text{O}_2\text{S}$	334
$\text{La}_2\text{O}_2\text{S}$	347

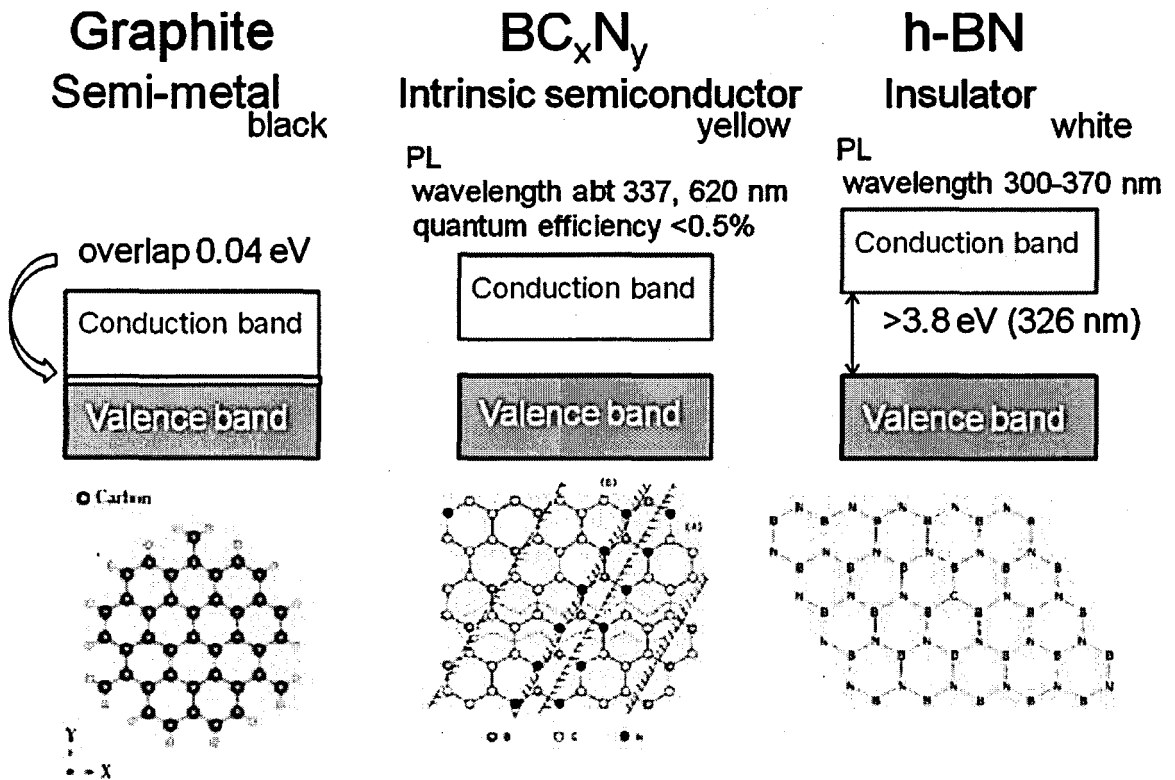


Fig.1.8 Schematic representation of Graphite, BC_xN_y , and h-BN photophysical characters and their structures.

Table.1.6 Photoluminescence wavelengths of BN/BCN

Material	PL wavelength peak (nm)	Reference
h-BN	300-350	Kanaev et al., 2004
h-BN, t-BN	370	Yang et al., 2006
BN	370	Kawaguchi et al., 1991
B ₂ CN	374	He et al., 2001
BCN nanotubes	370-470	Bai et al., 2000
BCN nano particle	430	Cao et al., 2003
BCN nano tube	400-500 520-600	Zhi et al., 2002
BC ₂ N	337	Guo et al., 2005
	620	Watanabe et al., 1996

h-BN = hexagonal Boron Nitride, t-BN = turbostratic Boron Nitride

BCN= Boron Carbon Nitride.

1.3.4 Control of Morphology

It is well known that, in the engineering of phosphors, there are three principal properties that must be both studied and controlled for the development of improved powder phosphors:

- (a) particle morphology and size (d_p);
- (b) stoichiometry and composition; and,
- (c) surface chemistry.

To use phosphors in high-resolution applications, fine spherical phosphor particles with both homogeneous composition and good surface properties are highly desirable. (Wang et al., 2007)

However, only a few studies of morphologic control have been reported. In this thesis, the morphology of the phosphors will be controlled to produce either solid or porous particles for the following reasons. Recently, porous materials have attracted increasing attention for their potential use in electrochemistry, nanomaterials, photonic crystals, and in drug delivery for determination of the efficiency of drug release. The advantages of porous materials include their high surface area, low density, and hierarchical structures. Similar to nanomaterials, the material properties of ordered porous particles are preserved on the submicrometer scale. However, ordered porous particles have advantages over nanomaterials: superior surface and thermal stability, ease of handling, and shape preservation.

We selected $Y_2O_3:Eu^{3+}$ as the model material. To prepare porous particles, a mixture of an yttrium and europium nitrate solution and colloidal polystyrene latex (PSL) particles was used as the precursor. The precursor was atomized into micrometer-sized droplets using an ultrasonic nebulizer. The droplets then underwent evaporation, precipitation, thermolysis, and solidification to form the final product. Example SEM images of both non-porous and porous particles are shown in Fig.1.9. PL characterization is discussed in detail in Chapter 3.

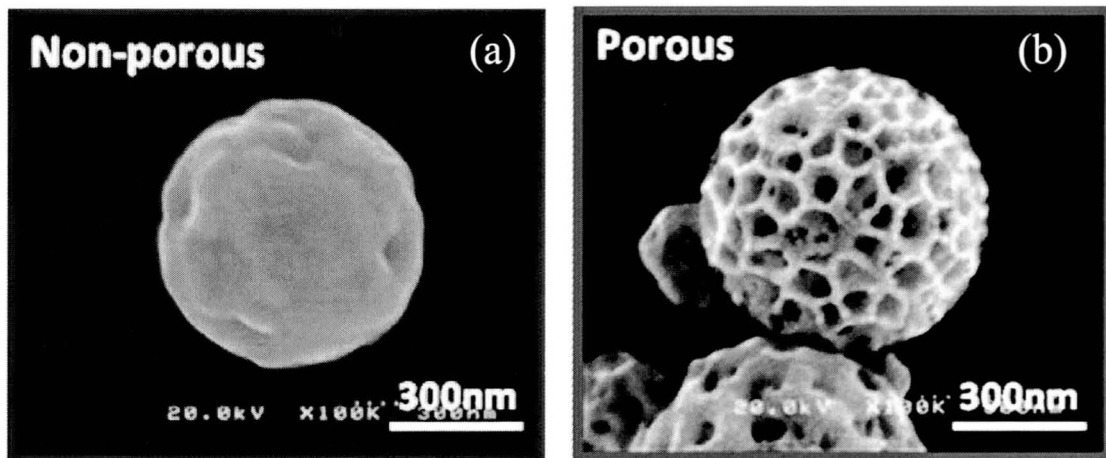


Fig. 1.9 SEM images of (a) non-porous and (b) porous particles.

1.4 Objectives

The primary objectives of this thesis are:

- 1) To investigate the relationship between photoluminescence and both the particle and crystallite size of the $\text{Y}_2\text{O}_3:\text{Eu}^{3+}$ fine particles;
- 2) To investigate the relationship between photoluminescence and the porosity of $\text{Y}_2\text{O}_3:\text{Eu}^{3+}$ phosphor fine particles; and,
- 3) To investigate the cause of the high luminescence of BCNO phosphors.

1.5 Outline of the Thesis

The thesis consists of five chapters. The organization of this thesis is shown in Fig.1.10.

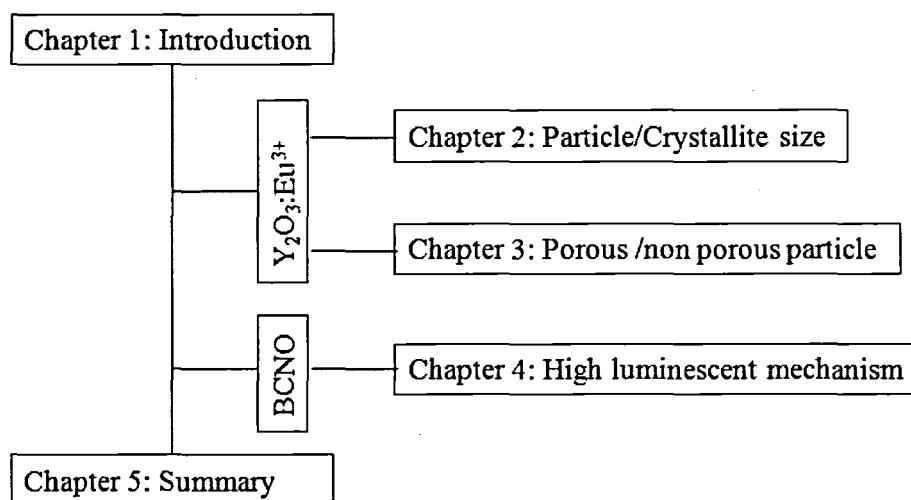


Fig. 1.10 Structure of chapters of present thesis

The objective of this thesis is to investigate the photoluminescence characterization and morphologic control of inorganic phosphor particles. Both solid/dense and porous particles of europium-doped yttrium oxide ($\text{Y}_2\text{O}_3:\text{Eu}^{3+}$), and newly synthesized carbon-based boron oxynitride (BCNO) phosphors were selected as model materials. The major conclusions of this thesis can be summarized as follows.

Chapter 1 discusses the background, previous research, methods used to investigate photoluminescence phenomena, current state of the field, and problems associated with

inorganic phosphors.

Chapter 2 describes the relationship between photoluminescence and both the particle and crystallite size of $\text{Y}_2\text{O}_3:\text{Eu}^{3+}$ fine particles. The crystallite and particle sizes played different roles in the control of the PL characteristics of the phosphors. The blue-shift of the charge transfer band in the excitation spectra was mostly due to the particle-size effect. In contrast, the decrease in the crystal symmetry ratio, which is the ratio of the C_2 to C_{3i} sub-lattice populations in the PL emission spectra, was primarily due to the effect of crystallite size.

Chapter 3 demonstrates the effect of porosity on the photoluminescence of $\text{Y}_2\text{O}_3:\text{Eu}^{3+}$ fine particles. The porous particles exhibited greater red-emission rendering properties than that of non-porous particles, based on the CIE chromaticity diagram. The photoluminescence intensity and quantum efficiency exhibited by the porous particles are greater than that of non-porous particles because the porous particles are hollow. Porous particles have unique photophysical properties, such as a 4-nm blue-shift in the charge-transfer and a lower symmetry ratio of 2.7, which were not exhibited by the non-porous particles with a particle size of 757 nm and a crystallite size of approximately 30 nm. The properties of sub-micrometer porous particles were identical to those of non-porous particles, which have reduced particle and crystallite size compared with porous particles.

Chapter 4 presents a detailed chemical analysis and photoluminescence characterization of the BCNO phosphors. The resulting powder has high external quantum efficiency with a direct band-gap transition. The BCNO phosphors have these properties because the atomic distances of the BCNO are less than those of conventional BCN compounds, which have an indirect band-gap transition and low quantum efficiency. The smaller atomic distances of the BCNO result from the presence of oxygen atoms, which have higher electron affinity and smaller covalent-bond radii compared with boron, carbon and nitrogen.

A simple summary and comments regarding future investigations are provided in **Chapter 5**.

References

- Abdullah, M., F. Iskandar, S. Shibamoto, T. Ogi and K. Okuyama, "Preparation of Oxide Particles with Ordered Macropores by Colloidal Templating and Spray Pyrolysis", *Acta Mater.* 52 (2004) 5151-5156
- Bai, X. D., E. G. Wang, and J. Yu, "Blue-violet Photoluminescence from large-scale highly aligned boron carbonitride nanofibers", *Appl. Phys. Lett.* 77 (2000) 67-69
- Bondeel, G., A. Harriman, G. Porter and A. Wilowska, "Photoredox process in metalloporphyrin-crown ether systems.", *J. Chem. Soc. Faraday Trans. 2*, 80 (1984) 867-876
- Cao., Z. X., and H. Oechsner, "Optical and mechanical characteristics of nanocrystalline boron carbonitride films synthesized by plasma-assisted physical vapor deposition", *J. Appl. Phys.*, 93 (2003) 1186-1189
- Chien, W. C., "Synthesis of $Y_2O_3:Eu$ phosphors by bicontinuous cubic phase process", *J. Cryst. Growth.*, 290 (2006) 554-559
- Endou, T., H. Iwasaki, T. Tsurumi, A. Nakahira, and H. Takizawa, "Introduction to Crystal Chemistry", Koudansha, Tokyo, (2000)
- Fleming, G. R., A. W. E. Knight, J. M. Morris R. J. S. Morrison and G. W. Rbionson, "Picosecond fluorescence studies of xanthenes dyes", *J. Am. Chem. Soc.*, 99 (1977) 4306-4311
- Fu., Z, S. Zhou, T. Pan, and S. Zhang, "Preparation and luminescent properties of cubic $Eu^{3+}:Y_2O_3$ nanocrystals and comparison to bulk $Eu^{3+}:Y_2O_3$ ", *J. Lumin.*, 124 (2007) 213-216
- Guo, Q., Y. Xie, C. Yi, L. Zhu, and P. Gao, "Synthesis of ultraviolet luminescent turbostratic boron nitride powders via a novel low-temperature, low-cost, and high-yield chemical route", *J. Solid State Chem.*, 178 (2005) 1925-1928
- Harriman, A., "Luminescence of porphyrins and metalloporphyrins.Part1.-Zinc(II), nickel(II) and manganese(II) porphyrins", *J. Chem. Soc. Faraday Trans.1*, 76 (1980) 1978-1985
- He, J. L., D. L. Yu, T. S. Wang, S. M. Liu, L. C. Guo, D. C. Li, X. P. Jia, L. X. Chen, G.

- T. Zou, and O. Yanagisawa, "Orthorombic B_2CN crystal synthesized by high pressure and temperature", *Chem. Phys. Lett.*, 340 (2001) 431-436
- Hong, G. Y., K. Yoo, S. J. Moon, and J. S. Yoo, "Enhancement of luminous intensity of spherical $Y_2O_3:Eu$ phosphors using flux during aerosol pyrolysis", *J. Electrochem. Soc.* 150 (2003) H67-H71
- Hunt Jr, R.B., and R. G Pappalardo, "Fast excited-state relaxation of Eu-Eu pairs in commercial $Y_2O_3:Eu^{3+}$ phosphors", *J. Lumin.* 34 (1985) 133-146
- Jing, X., T. Ireland, C. Gibbons, D. J. Barber, J. Silver, A. Vecht, G. Fern, P. Trowga, and D. C. Morton, "Control of $Y_2O_3:Eu$ spherical particle phosphor size, assembly properties, and performance for FED and HDTV", *J. Electrochem. Soc.* 146 (1999) 4654-4658
- Jones, S.L., R. K. Singh, and P. H. Holloway, "Luminescence of pulsed laser deposited Eu doped yttrium oxide films", *Appl. Phys. Lett.* 71 (1997) 404-406
- Jung, K.Y., C. H. Lee, Y. C. Kang., "Effect of surface area and crystallite size on luminescent intensity of $Y_2O_3:Eu$ phosphor prepared by spray pyrolysis", *Matter. Lett.*, 59 (2005) 2451-2456
- Kanaev, A.V, J-P. Petitet, L. Museur, V. Marine, V. L. Solozhenko and V. Zafirooulos, "Femtosecond and ultraviolet laser irradiation of graphite like hexagonal boron nitride", *J. Appl. Phys.*, 96 (2004) 4483-4489
- Kang, Y. C. S. B. Park, I. W. Lenggoro, and K. Okuyama, "Preparation of non-aggregated $Y_2O_3:Eu$ phosphor particles by spray pyrolysis Method", *J. Mater. Res.*, 14 (1999), 2611-2615
- Kang, Y. C., H. S. Roh, and S. B. Park, "Preparation of $Y_2O_3:Eu$ Phosphor particles of filled morphology at high precursor concentrations by spray pyrolysis", *Adv. Mater.* 12 (2000) 451-453
- Kawaguchi., M., K. Nozaki, Y. Kita, and M. Doi, "Photoluminescence characteristics of $BN(C,H)$ prepared by chemical vapour deposition", *J. Mater. Sci.*, 26 (1991) 3926-3930
- Kobayashi, H., "Luminescence Physics", Asakura pub. 2000.
- Kottaisamy, M., D. Jeyakumar, R. Jagannathan, and M. M. Rao, " $Yttrium\ oxide:Eu^{3+}$ "

- red phosphor by self-propagating high temperature synthesis”, *Mater. Res. Bull.* 31 (1996) 1013-1020
- Lackowicz, J.R. ed. “Topics in Fluorescence Spectroscopy Vol.1. Techniques”, Plenum Press, New York, 1991
- Lampert, R. A., L. A. Chewter and D. Phillips, “Standards for nanosecond fluorescence decay time measurements”, *Anal. Chem.*, 55(1983) 68-78
- Lenggoro, I. W., and K. Okuyama, “Preparation of Fine Phosphor and Luminescent Micro/Nanoparticles Using Spray Pyrolysis. In Handbook of Luminescence, Display Materials, and Devices – Inorganic Display Materials, H. S. Nalwa and L. S. Rohwer, Eds., American Scientific Publishers: Stevenson Ranch, California, (2003) Vol.2. P327.
- Liu. G., and B. Jacquier (eds). “Spectroscopic Properties of Rare Earths in Optical Materials”, Springer, 2005
- Martinez-Rubio, M.I., T. G. Ireland, G. R. Fern, J. Silver, and M. J. Snowden, “A new application for microgels: novel method for the synthesis of spherical particles of the $Y_2O_3:Eu$ phosphor using a copolymer microgel of NIPAM and acrylic acid”, *Langmuir* 17 (2001) 7145-7149
- Minami, T., and S. Hirayama, “High quality fluorescence decay curves and lifetime imaging using an elliptical scan streak camera”, *J. Photochem. Photobio, A: Chemistry*, 53 (1990) 11-21
- Minami, T., M. Kawahigashi, Y. Sakai, K. Shimamoto, and S. Hirayama, “Fluorescence lifetime measurements under microscope by the time-correlated single-photon counting technique”, *J. Lumin* 35 (1986) 247-253
- Minami, T., W-N. Wang, F. Iskandar, and K. Okuyama, “Photoluminescence properties of submicrometer phosphors with different crystallite/particle sizes”, *Jpn.J.Appl.Phys.* 47 (2008) 7220-7223
- O’Conner., D. V, and D. Phillips, “Time-correlated single-photon counting”, Academic Press, London, (1985)
- Osuka, A., S. Morikawa, K. Maruyama, S. Hirayama and T. Minami, “An efficient photochemical synthesis of conformationally restricted quinone-substituted

- porphyrins”, J. Chem. Soc. Chem. Commun.(1987) 359-361
- Rodgers, M. A., “Fluorescence spectroscopy with picoseconds time resolution”, Optical Engin., 22 (1983) 521-526
- Sakai, Y., M. Kawahigashi, T. Minami, T. Inoue, and S. Hirayama, “Deconvolution of non-exponential emission decays arising from reabsorption of emitted light”, J. Lumin 42 (1989) 317-324
- Stich, M.L., “Laser Handbook”, vol 3, North Holland Pub.Co., 1979, p.844
- Silver, J. M. I. Martinez-Rubio, T. G. Ireland, G. R. Fern, and R. Withnall, “The effect of particle morphology and crystallite size on the upconversion luminescence properties of erbium and ytterbium Co-doped yttrium oxide phosphors”, J. Phys. Chem. B. 105 (2001) 948-953
- Turro, N.J., “Modern Molecular Photochemistry”, Benjamin/Cummings Pub. (1978)
- van Pieterse, L., M. F. Reid, R. T. Wegh, S. Soverna, and A. Meijerink., “ $4f^n \rightarrow 4f^{n-1}5d$ transitions of the light lanthanides: Experiment and theory”, Phys. Rev. B 65 (2002) 045113-045128
- van Pieterse, L., M.Heeroma, E. de Heer, and A. Meijerink, “Charge transfer luminescence of Yb^{3+} ”, J. Lumin. ,91 (2000) 177-193
- Wan, J. X., Z. H. Wang, X.Y. Chen, L. Mu, and Y. T. Qian, “Shape-tailored photoluminescent intensity of red phosphor $\text{Y}_2\text{O}_3:\text{Eu}^{3+}$ ”, J. Cryst. Growth, 284 (2005) 538-543
- Wang, W-N., W. Widiyastuti, I. W. Lenggoro, T. O. Kim, and K. Okuyama, “Photoluminescence optimization of luminescent nanocomposites by spray pyrolysis of a colloid-solution Precursor”, J. Electrochem. Soc. 154 (2007) J121-J128
- Ware, W. R., M. Pratinidhi and R. K. Bauer, “Performance characteristics of a small side-window photomultiplier in laser single-photon fluorescence decay measurements”, Rev. Sci. Instrum., 54 (1983) 1148-1156
- Watanabe, M.O, S. Itoh, T. Sasaki, and K. Mizushima, “Visible-light-emitting layered BC_2N semiconductor”, Phys. Rev. Lett., 77 (1996) 187-189
- Widiyastuti, W., T. Minami, W-N. Wang, F. Iskandar, and K. Okuyama,

“Photoluminescence characteristics of ordered macroporous Eu-doped yttrium oxide particles prepared by spray pyrolysis”, *Jpn.J.Appl.Phys.* in press

Wu, Z. J., and S. Y. Zhang, “Semi empirical method for the evaluation of bond covalency in complex crystals”, 103 (1999) 4270-4274

Xia, B., I. W. Lenggoro, and K. Okuyama, “Synthesis and photoluminescence of spherical ZnS:Mn²⁺ particles”, *Chem. Mater.* 14 (2002) 4969-4974

Yang, J., T. Qiu, and C-Y. Shen, “New BCN fibers for strong ultraviolet and visible light luminescence”, *Chin. phys.*, 23(2006) 2573-2575

Yokoyama, I., K. Tarui, and T. Minami, “Application of time resolved photospectrometer”, *Optronics*, 2 (1992) 82-86

Zhang, J.Y, Z. T. Zhang, Z. L. Tang, Y. H. Lin, and Z. S. Zheng, “Luminescent properties of Y₂O₃:Eu synthesized by sol-gel processing”, *J. Mater. Process. Technol.*, 121 (2002) 265-268

Zhi, C.Y., J. D. Guo, X. D. Bai and E. G. Wang, “Adjustable boron carbonitride nanotubes”, *J. Appl. Phys.*, 91 (2002) 5325-5334

Chapter 2

Photoluminescence Properties of Submicrometer Phosphors with Different Crystallite/Particle Sizes

2.1 Introduction

Rare earth doped inorganic phosphors are of technological importance because they are widely used in color displays and fluorescent lamps, due to their sharp color rendering properties. Microcrystalline yttrium oxide doped with Eu^{3+} ($\text{Y}_2\text{O}_3:\text{Eu}^{3+}$) represents a typical example and is considered to be one of best red phosphors currently available.

The spray pyrolysis method is potentially promising, since it is a rapid, continuous, low cost process and can be used in the fabrication of diverse materials, including phosphors, with controllable size and compositions (Kang et al., 1999; Xia et al. 2002). Particles prepared using the conventional spray pyrolysis (CSP) method are highly uniform in size and composition, with a spherical morphology, and have non-agglomeration characteristics, because of the microscale reactions that proceed inside each droplet.

Wang et al., (2007) reported a systematic experimental study regarding the effects of particle size/crystallinity, chemical composition, and surface properties on the photoluminescence (PL) intensity of submicrometer dense $\text{Y}_2\text{O}_3:\text{Eu}^{3+}$ particles by a spray pyrolysis method. However, a detailed investigation of the effects of particle/crystallite sizes on the PL properties, in particular the excitation spectra, was not carried out, and these effects are considered to be very important to an

understanding of the properties of submicrometer phosphor particles.

In this study, further investigations into the effects of the crystallite and particle sizes were carried out, by studying the charge transfer (CT) band shift in the excitation spectra and the variation of crystal symmetry ratio of C_2 to C_{3i} in the emission spectra.

2.2 Experimental Procedure

Aqueous solutions of yttrium nitrate ($Y(NO_3)_3 \cdot 6H_2O$) and europium nitrate ($Eu(NO_3)_3 \cdot 6H_2O$) were used as precursors. Europium atoms were added, to a doping level of 6 mol% relative to that of yttrium atoms. All chemicals were purchased from Kanto Chemical Co., Tokyo, and were used without further purification. The solutions were then atomized by means of an ultrasonic nebulizer operated at 1.7 MHz (NE-U17, Omron Co., Tokyo), and the mist was carried by air at 2 L/min into a tubular alumina reactor ($L = 1$ m, $I.D. = 30$ mm) maintained at predetermined temperatures. The aerosol products were collected in an electrostatic precipitator. The CSP setup has been described in detail in our previous papers (Kang et al., 1999; Wang et al., 2007).

The morphology and grain size of the resulting particles were examined using field-emission scanning microscopy (FE-SEM, S-5000, Hitachi Corp., Tokyo). Crystalline phases were characterized by X-ray diffraction (XRD, RINT 2200V, Rigaku Denki, Tokyo). Crystallite size was calculated using the Scherrer equation. The calculation was based on the measurement of full-width at half-maximum (FWHM) values of the peak (222) at 29.1° in the corresponding XRD patterns. PL spectra of the phosphors were recorded at room temperature by means of a spectrofluorophotometer (RF-5300PC, Shimadzu Corp., Kyoto) excited at 254 nm with the band width resolution less than 3 nm and the S/N higher than 150.

2.3 Results and Discussion

To examine the effect of crystallite size, precursors with the same concentration, 0.10 M, were atomized to prepare phosphor particles at various synthesis temperatures ranging from 800°C to 1400°C . On the other hand, to investigate the particle size effect,

precursors with different concentrations, 0.01 – 0.20 M, were sprayed at a constant synthesis temperature (1400°C). The sizes of the resulting particles were in the range of 390 to 940 nm, following the one-droplet-to-one-particle (ODOP) principle. This approach for independent control of particle and crystallite sizes in the spray route was described in detail in our previous work (Wang et al., 2007).

2.3.1 Morphology, Particle Size, and Crystallinity Characterization

FE-SEM images of the resulting $\text{Y}_2\text{O}_3:\text{Eu}^{3+}$ submicrometer particles are shown in Figs. 2.1 and 2.2. It can be seen from these images that all samples obtained via the spray route were non-agglomerated spherical particles, which is considered to be beneficial in enhancing PL properties. When precursors with the same concentration were sprayed at various synthesis temperatures, the product particle sizes remained nearly constant at around 900 nm (see Fig.2.1). For example, the particle sizes were 920, 1040, 880, and 940 nm at 800°C, 1000°C, 1200°C, and 1400°C, respectively. The slight variation in particle size was due to the sampling error from their corresponding SEM images.

XRD patterns of the resulting particles are presented in Figs. 2.1 and 2.2 as well. The diffraction peaks of 2θ were observed at 20.5, 29.1, 33.8, 35.9, 40.0, 43.5, 48.6, 53.2, and 57.7, which can be indexed to the pure body-centered cubic (bcc) Y_2O_3 phase. No impurity peaks and no transition to monoclinic phases were observed, indicating that the particles were pure in both chemistry and crystalline phase. The crystallite size was calculated from XRD patterns using the Scherrer equation. As seen in Fig. 2.1, the crystallite size was calculated to range from 16.4 nm at 800°C to 37.3 nm at 1400°C. This was due to the higher energy supply from the high synthesis temperature, which improved nucleation and crystallite growth. On the other hand, when precursors with various concentrations were sprayed at 1400°C, the crystallinity did not vary significantly since the energy supply was constant. From Fig. 2.2, for example, the crystallite size of the particles is relatively constant at around 35 nm. The slight difference in crystallite size was caused by differences in energy receiving of precursors at various concentrations.

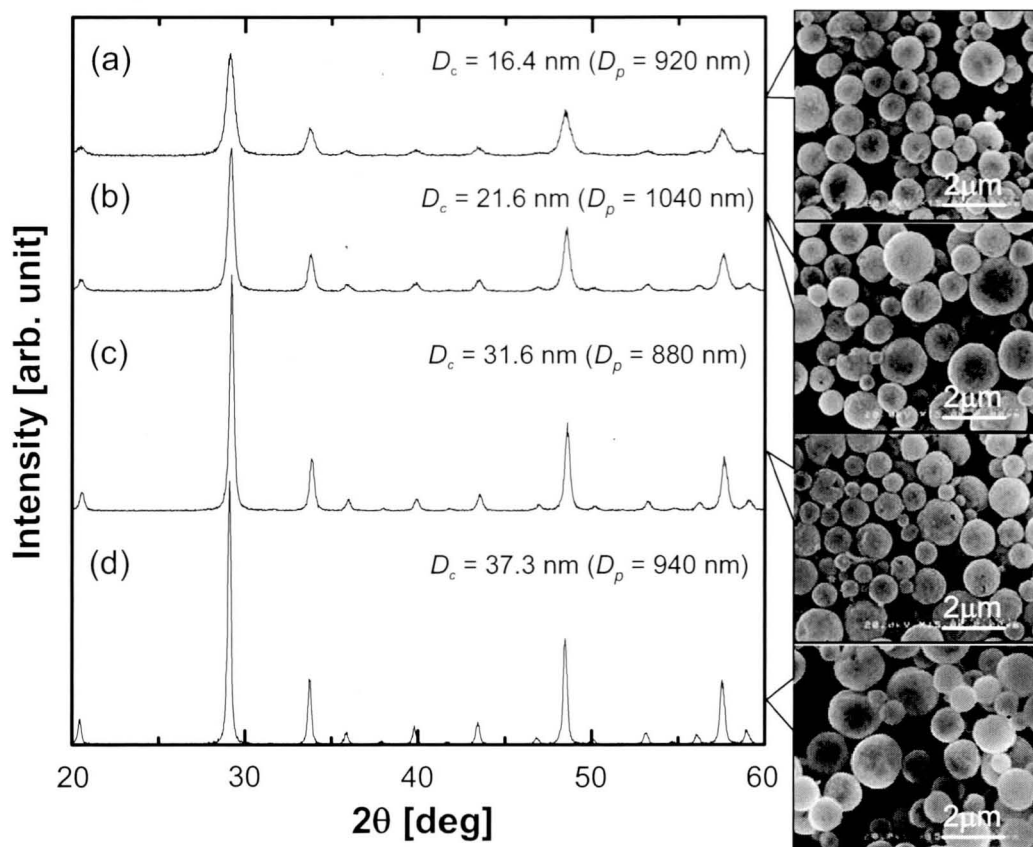


Fig. 2.1 XRD patterns (left) and FE-SEM images (right) of $\text{Y}_2\text{O}_3:\text{Eu}^{3+}$ particles prepared from 0.1 M precursor at (a) 800°C, (b) 1000°C, (c) 1200°C, and (d) 1400°C.

The average particle sizes (D_p) are nearly constant at around 900 nm.

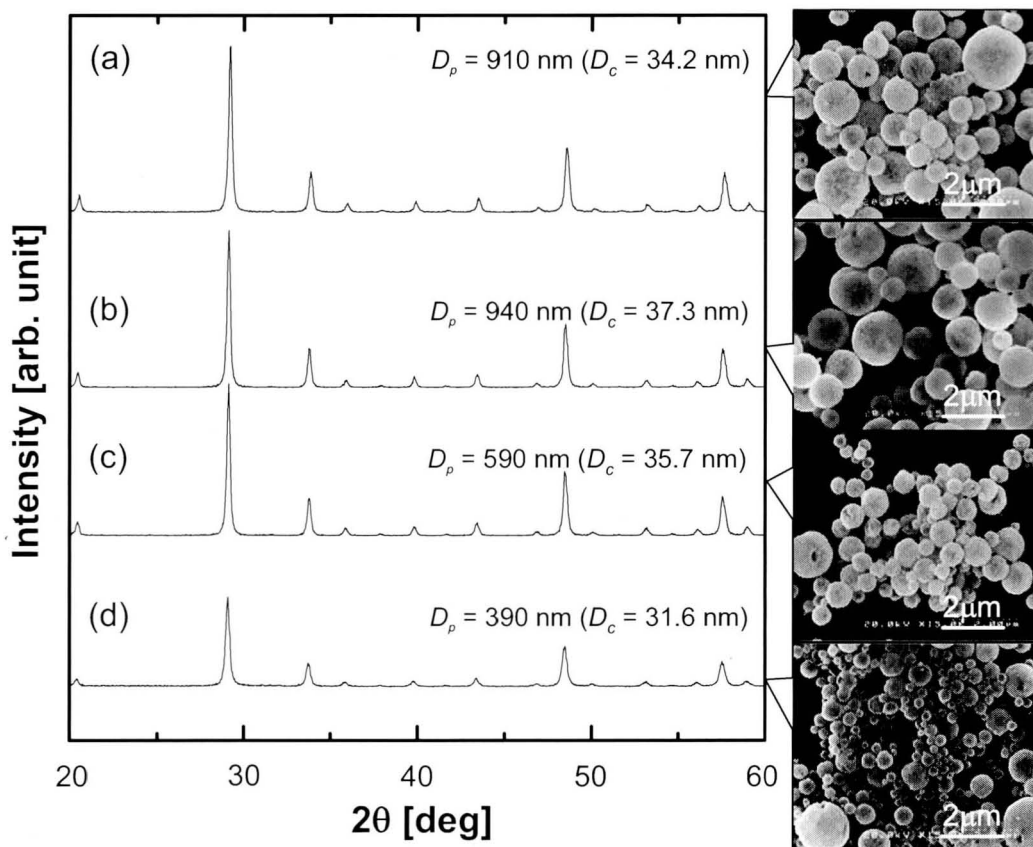


Fig. 2.2 XRD patterns (left) and FE-SEM images (right) of $\text{Y}_2\text{O}_3:\text{Eu}^{3+}$ particles prepared from precursors with different concentrations (a) 0.20 M, (b) 0.10 M, (c) 0.05 M, and (d) 0.01 M at 1400°C . The average crystallite sizes (D_c) are nearly constant at around 35 nm.

2.3.2 Excitation Spectra Characterization

The excitation spectra of $\text{Y}_2\text{O}_3:\text{Eu}^{3+}$ particles prepared at different synthesis temperatures and precursor concentrations, representing different crystal sizes and particle sizes, respectively, are shown in Fig. 2.3. These excitation spectra were measured at an emission of 612 nm (Hunt et al., 1985).

The broad excitation spectrum peak located at around 250 nm is assigned to the excited charge-transfer (CT) band of Eu^{3+} . The CT band of $\text{Y}_2\text{O}_3:\text{Eu}^{3+}$ corresponds to the electronic transition from the 2p orbital of O^{2-} to the 4f orbital of Eu^{3+} and is closely related to the covalency between O^{2-} and Eu^{3+} and the coordination environment around Eu^{3+} (Wang et al., 2007). The first factor to be mentioned is covalency. For increasing covalency the interaction between the electrons is reduced, since they spread out over wider orbitals. Consequently, electronic transitions between energy levels with an energy difference that is determined by electron interaction shift to lower energy, i.e., larger wavelength (red shift), for increasing covalency. Another factor responsible for the influence of the host lattice on the optical properties of a given ion is the crystal field. This is the electric field at the site of the ion under consideration due to the surroundings (Blasse et al., 1994)

In Fig. 2.3, a blue shift of the CT band was observed. Van Pieteron *et al.* reported that the peak wavelength shift of the CT band by different host crystals, such as Y_2O_3 , $\text{Y}_2\text{O}_2\text{S}$, YPO_4 , etc., is determined by the nature of the ligand, the metal ion, the coordination and the size of cation site (van Pieteron et al., 2000). In $\text{Y}_2\text{O}_3:\text{Eu}^{3+}$ the CT band is closely related to the covalence between O^{2-} and Eu^{3+} and the coordination environment around Eu^{3+} . The Eu-O distance is the main factor that influences the CT band position. When the Eu-O distance becomes shorter, the crystal field splitting becomes larger, and the energy from the valence band to the CT band increases, leading to the blue shift of the CT band. Fu *et al.* also reported that the CT band of $\text{Y}_2\text{O}_3:\text{Eu}^{3+}$ nanocrystals, prepared by a combustion method, showed a 7 nm blue shift compared with that of bulk material (Fu et al., 2007). However, only the effect of crystallite size, not that of particle size, was considered in that study.

The CT band peak wavelengths as a function of crystallite/particle sizes of the

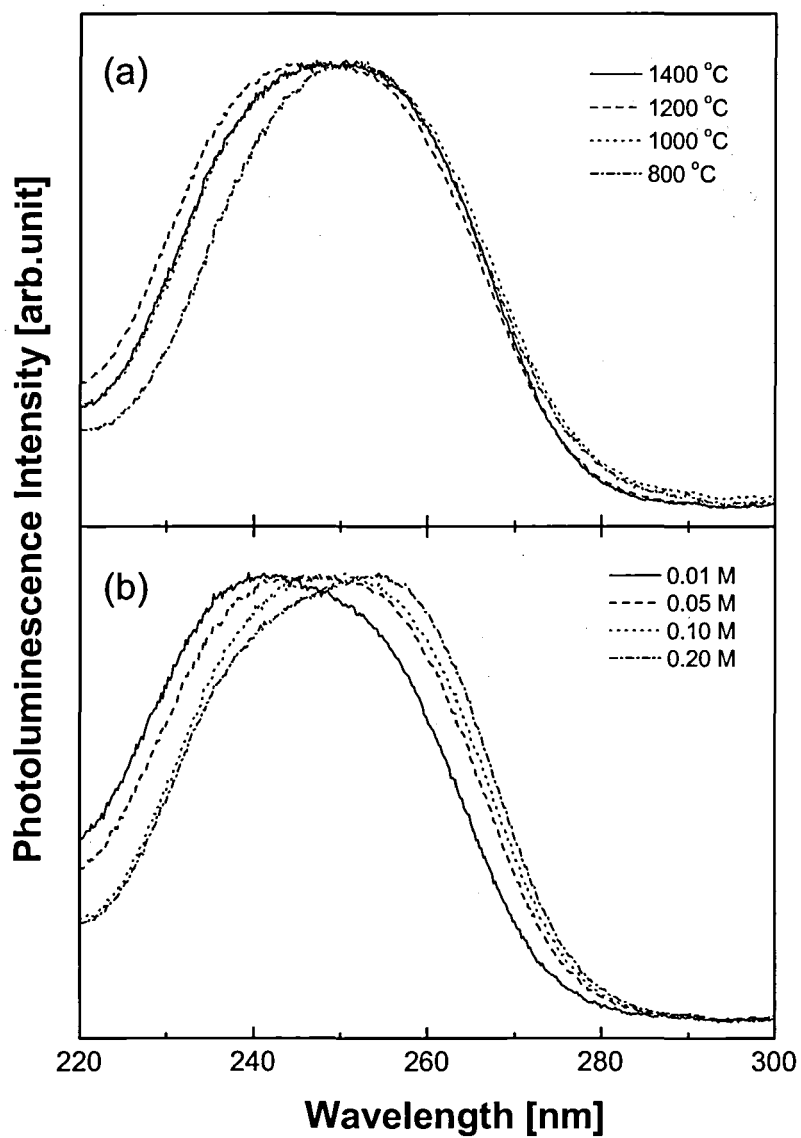


Fig. 2.3 Excitation spectra of $\text{Y}_2\text{O}_3:\text{Eu}^{3+}$ particles with (a) different crystallite sizes and (b) different particle sizes.

$\text{Y}_2\text{O}_3:\text{Eu}^{3+}$ particles prepared in this study are shown in Fig. 2.4. In Fig. 2.4(a), the CT band peak wavelengths were almost constant at different crystallite sizes. The slight variation in the bandwidth was caused by the difference in particle size, as discussed above. This phenomenon can be explained as follows. It has been reported that the CT state of Eu^{3+} can be created by receiving one electron from its ligand, i.e., oxygen. A submicrometer particle prepared by the spray pyrolysis method is actually an aggregate of many primary nanocrystallites. The surfaces of these crystallites may have defects that can absorb CO_2 and H_2O from the atmosphere (Wang et al., 2007; Song et al., 2003a). When the lattice defect is located in the crystallite boundary, Eu^{3+} has no proper ligands, and Eu^{3+} cannot reach the CT state. In this case, the Eu-O distance may have only a minor influence. Therefore, the crystallite size shows no significant effect on the peak wavelength shift of the CT band.

However, the plot of the CT band peak wavelength and the particle size followed a linear relationship, as shown in Fig. 2.4(b). A 6 nm blue shift of the CT band peak wavelength at the particle size of 390 nm was observed, compared with that of bulk material. The effect of the blue shift in this case was due to the bond length of Eu-O and its bond covalency. Fu et al. 2007 reported that the energy band-gap in Y_2O_3 base crystal in the submicrometer particles is higher than that of bulk state by band energy calculation using the first-principles. The distance of Y-O, hence the Eu-O, becomes shorter with the decreasing grain size.

Thus we can conclude that the CT band peak wavelength is dependent on the particle size, but independent of the crystallite size.

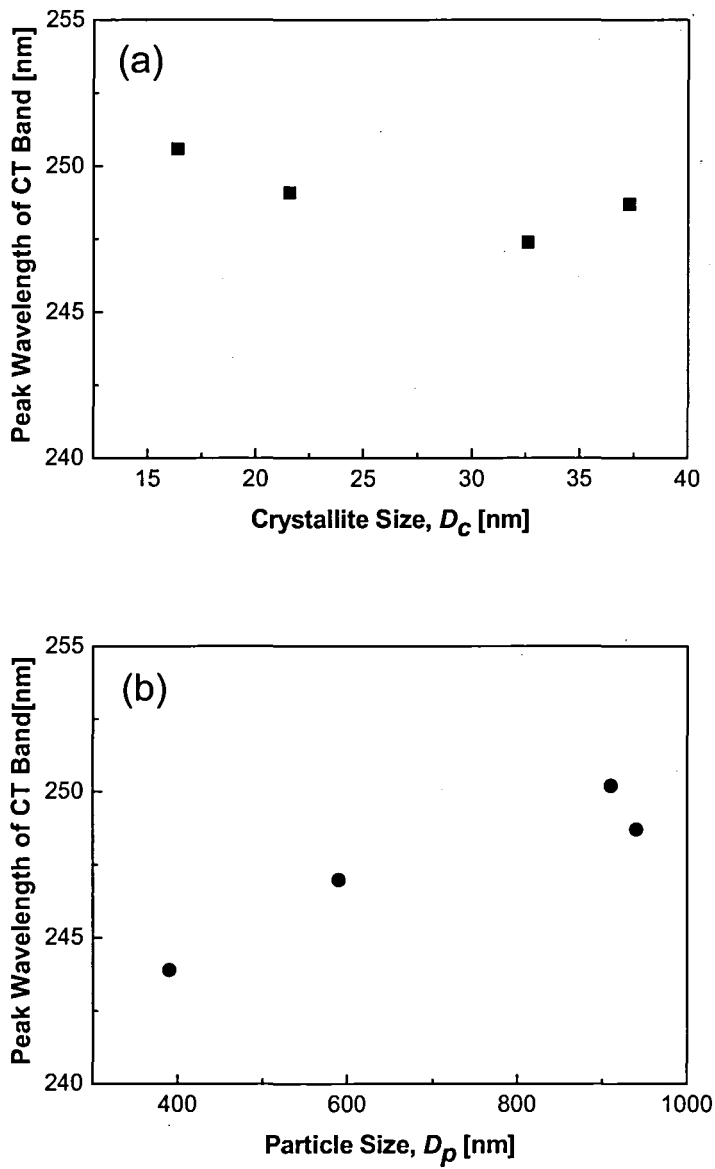


Fig. 2.4 The excitation wavelength as a function of (a) crystallite size and (b) particle size of $\text{Y}_2\text{O}_3:\text{Eu}^{3+}$ particles.

2.3.3 Emission Spectra Characterization

Figure 2.5 shows PL emission spectra of the $\text{Y}_2\text{O}_3:\text{Eu}^{3+}$ particles with different crystallite sizes (a) and particle sizes (b), which were recorded under excitation at 254 nm. The emission lines of Eu^{3+} are assigned to ${}^5\text{D}_0$ to ${}^7\text{F}_J$ ($J=0, 1, 2, 3, 4, 5, 6$, not in all cases). It is well known that rare earths doped in yttrium oxide incorporate into two non-equivalent crystal sites having different symmetries of C_2 and C_{3i} (also called S_6) (Wang et al., 2007; Hunt et al., 1985). A total of 75% of these sites are noncentrosymmetric having a C_2 symmetry, and the remaining 25% are centrosymmetric having C_{3i} symmetry (Wang et al., 2007). Due to the presence of a center of symmetry, only magnetic transitions (selection rule $\Delta J=0, \pm 1, J=0 > J=0$ forbidden) are allowed for the $\text{Eu}^{3+}(\text{C}_{3i})$ ion. These wavelength lines, ranging from 580 to 600 nm, are listed according to Hunt et al. 1985 in Fig. 2.5. PL emission peaks from Eu^{3+} at 587.7 nm (${}^5\text{D}_0(\text{C}_2) \rightarrow {}^7\text{F}_{1a}(\text{C}_2)$) and 582.4 nm (${}^5\text{D}_0(\text{C}_{3i}) \rightarrow {}^7\text{F}_{1a}(\text{C}_{3i})$) were transformed from the C_2 and C_{3i} sites, respectively, because the ${}^5\text{D}_0$ level for the C_2 site is predicted to be 87 cm^{-1} lower in energy than the ${}^5\text{D}_0$ level of the C_{3i} sub-lattice, and the ${}^7\text{F}_{1a}$ level for the C_2 site is predicted to be 69.4 cm^{-1} higher in energy than the ${}^7\text{F}_{1a}$ level of the C_{3i} sub-lattice (Hunt et al., 1985). The ratio of PL emission peak intensity at 587.7 nm to that at 582.4 nm thus exhibited the symmetry ratio of C_2 to C_{3i} sub-lattice. The ratio around 3 indicates that there is no preferential occupation by Eu^{3+} of the C_2 and C_{3i} sites (Sato et al., 2005; Haber et al., 1973).

In our previous work (Wang et al., 2007), we have reported the correlations between the PL peaks and the particle/crystallite sizes. The PL intensity has a linear relationship between crystallite sizes from 10 nm to 50 nm, and has a constant value over 50 nm. In this region, the PL intensity increased twice from the crystallite size of 15 nm to 50 nm. The same results were observed in Fig.2.5(a), where the PL intensity doubled from the prepared temperatures of 800°C to 1400°C , corresponding to the crystallite sizes from 16.4 nm to 37.3 nm. The PL intensity and particle size have another relationship. The particles with the size of 500 nm have the PL intensity three times that of 200 nm, and they reached a constant value from 500 nm to around 900 nm (Wang et al., 2007). In Fig.2.5(b), we showed the same relationship between the PL intensity and the particle

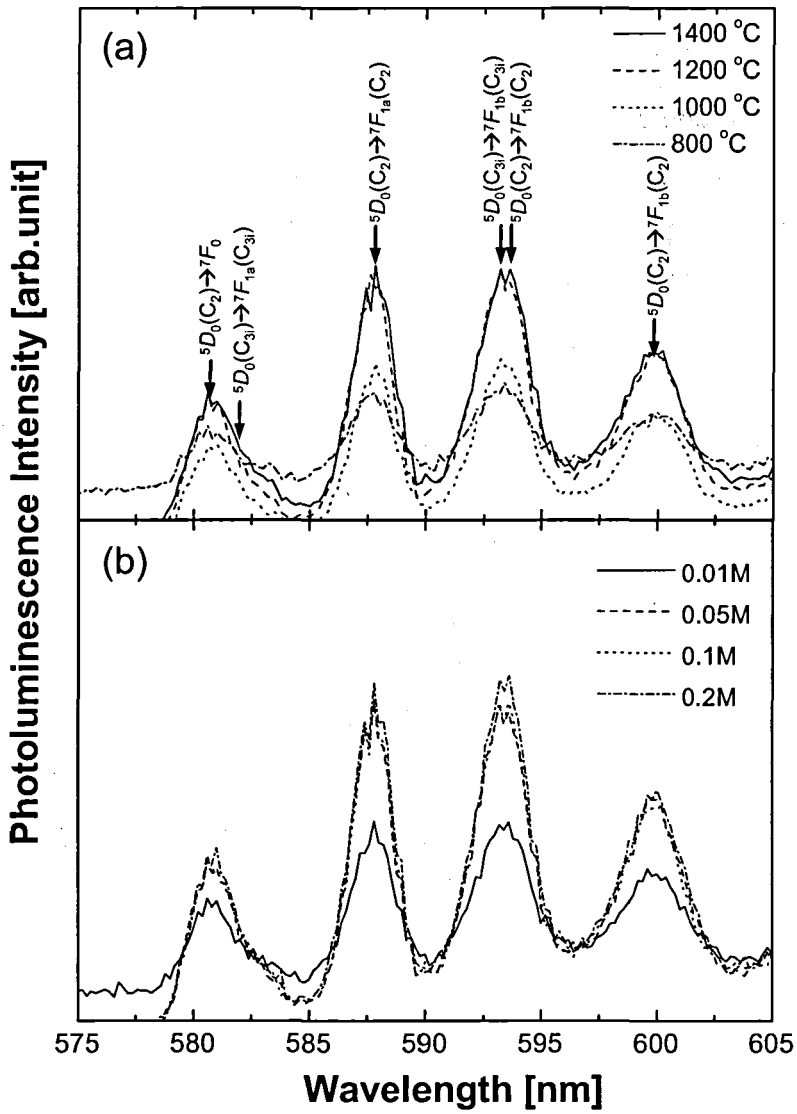


Fig. 2.5 Emission spectra of $\text{Y}_2\text{O}_3:\text{Eu}^{3+}$ particles with (a) different crystallite sizes and (b) different particle sizes, respectively.

size, i.e., the PL intensity increased with increasing particle size.

Figure 2.6 shows the relationships between the symmetry ratio of C_2 (at 587.7nm) to C_{3i} (at 582.4nm) and different crystallite/particle sizes. In Fig. 2.6(a), the symmetry ratios increased with the crystallite size from 16.4 nm to 31.6 nm, and then decreased. The ratio for the crystallite size larger than 20 nm was around 3, indicating a non-preferential condition of Eu^{3+} . For the crystallite size smaller than 16.4 nm, the ratio of C_2 to C_{3i} was less than 3, which is not a preferential condition compared with that in bulk materials.

As discussed above, more atoms are located on the particle surface of submicrometer particles, compared with bulk materials, and the surface defects of the crystallite may occur to a greater degree. These defects may increase the degree of disorder and lower the local symmetry of Eu^{3+} ions located near the surface (Song et al., 2003b). This lower local symmetry may lead to differences in the intensity ratio of $\text{Y}_2\text{O}_3:\text{Eu}^{3+}$ phosphor particles. As explained before, spray pyrolyzed particles are aggregates of nanocrystallites with amorphous phase and defects (Wang et al., 2007). These amorphous/defected parts exhibit local distortion on some of the sites around Eu^{3+} , causing the symmetry ratio to differ from 3. However, in Fig. 2.6(b), the symmetry ratios for different particle sizes were almost constant. This means that the particle size does not affect the ratio of C_2 to C_{3i} , since the amorphous/defect parts are located around the crystallite surfaces, not around the particle surfaces.

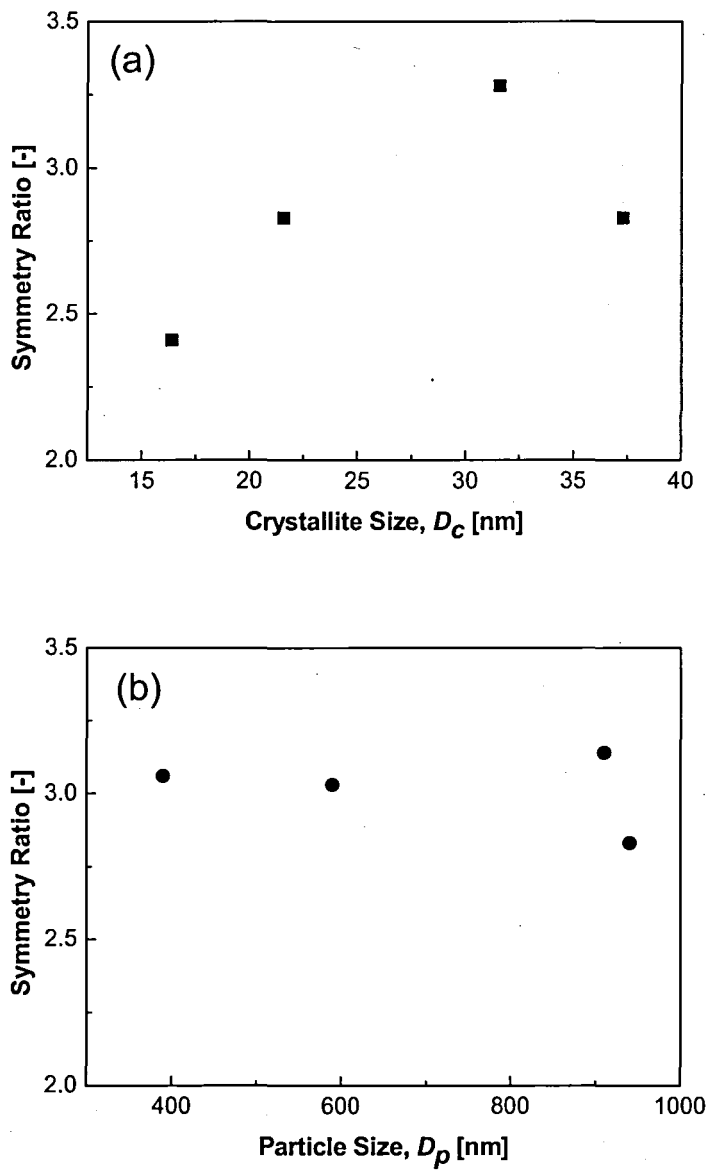


Fig. 2.6 The symmetry ratio of C_2 (at 587.7nm) to C_{31} (at 582.4nm) as a function of (a) crystallite size and (b) particle size of $\text{Y}_2\text{O}_3:\text{Eu}^{3+}$ particles.

2.4 Summary

The effects of crystallite and particle sizes on the CT band in the excitation spectra and PL emission characteristics of submicrometer $\text{Y}_2\text{O}_3:\text{Eu}^{3+}$ were investigated. The resulting phosphor particles were analyzed with CT band spectra and PL emission spectra. The results showed that the blue wavelength shift of the CT band peak for the submicrometer particles is dependent mainly on the particle size, since the dominant factor, Eu-O distance, is dependent on the particle size. On the other hand, the crystal symmetry occupation ratio of C_2 to C_{3i} is dependent on the crystallite size, since the dominant factor, the surface defect, exists on the crystallite surfaces.

References

- Blasse, G. and B. C. Grabmaier: *Luminescent Materials*, (Springer-Verlag, Berlin, 1994), p.17-19.
- Fu., Z, S. Zhou, T. Pan, and S. Zhang, "Preparation and luminescent properties of cubic $\text{Eu}^{3+}:\text{Y}_2\text{O}_3$ nanocrystals and comparison to bulk $\text{Eu}^{3+}:\text{Y}_2\text{O}_3$ ", *J. Lumin*, 124 (2007) 213-216
- Heber, J. and U. Köbler: in *Luminescence of Crystals, Molecules and Solutions*, ed. F. Williams (Plenum Press, New York, 1973) p.379.
- Hunt Jr, R.B., and R. G. Pappalardo, "Fast excited-state relaxation of Eu-Eu pairs in commercial $\text{Y}_2\text{O}_3:\text{Eu}^{3+}$ phosphors", *J. Lumin*. 34 (1985) 133-146
- Kang, Y.C. S. B. Park, I.W. Lenggoro, and K. Okuyama, "Preparation of non-aggregated $\text{Y}_2\text{O}_3:\text{Eu}$ phosphor particles by spray pyrolysis", *Method. J. Mater. Res.*, 14 (1999), 2611-2615 .
- Satoh, Y., H. Najavov, S. Ohsio and H. Saitoh, "Luminescence Properties from C_2 Site of C-Type Cubic $\text{Y}_2\text{O}_3:\text{Eu}$ Whiskers", *Adv. Technol. Mater. Mater. Process*. 17 (2005) 43-46
- Song, H. , B. Chen, B. Sun, J. Zhang, and S. Lu, "Ultraviolet light-induced spectral change in cubic nanocrystalline $\text{Y}_2\text{O}_3:\text{Eu}^{3+}$ ", *Chem. Phys. Lett*. 372 (2003a) 368-372
- Song, H., J. Wang, B. Chen, H. Peng, and S. Lu, "Size-dependent electronic transition rates in cubic nanocrystalline europium doped yttria", *Chem. Phys. Lett*. 376 (2003b) 1-5
- van Pieteron, L., M. Heeroma, E. de Heer, and A. Meijerink, "Charge transfer luminescence of Yb^{3+} ", *J. Lumin*. ,91 (2000) 177-193.
- Wang, W-N., W. Widiyastuti, T. Ogi, I. W. Lenggoro, and K. Okuyama, "Correlations between Crystallite/Particle Size and Photoluminescence Properties of Submicrometer Phosphors", *Chem. Mater*. 19 (2007) 1723-1730
- Xia, B., I. W. Lenggoro, and K. Okuyama, "Synthesis and photoluminescence of spherical $\text{ZnS}:\text{Mn}^{2+}$ particles", *Chem. Mater*. 14 (2002) 4969-497

Chapter 3

Photoluminescence Characteristics of Ordered Macroporous Eu-doped Yttrium Oxide Particles Prepared by Spray Pyrolysis

3.1 Introduction

Rare earth doped phosphor materials have been used in many applications such as field emission display, cathode ray tube, and plasma display panels. Among these materials, europium-doped yttrium oxide ($\text{Y}_2\text{O}_3:\text{Eu}^{3+}$) is one of the most promising red phosphors due to its stability under vacuum, high thermal conductivity and high melting point (Wang et al., 2007a; Jones et al, 1997). Mostly non-porous $\text{Y}_2\text{O}_3:\text{Eu}^{3+}$ particles, i.e., dense/filled particles, can be prepared using a variety of methods, and the corresponding photoluminescence (PL) characteristics of the particles with regard to different factors, such as morphology, particle size, crystallinity, and composition, have been investigated (Wang et al., 2007a; Jones et al., 1997, Shea et al., 1998; Joffin et al., 2005, Minami et al., 2008).

In contrast, porous materials recently have attracted increasing attention for applications in electrochemistry (Wang,F. et al., 2007), nanomaterials (Wang, H.Q. et al., 2007; Liu et al.,2006), photonic crystals (Yan et al., 2005), and drug delivery for tracking the efficiency of the drug release owing to their high surface area, low density, and hierarchical structures (Yang et al., 2007). Similar to nanomaterials, ordered porous

particles maintain material properties on the submicrometer scale. However, ordered porous particles have advantages over nanomaterials: superior surface and thermal stability, easy handling and shape preservation (Okuyama et al., 2006).

Recently, our group reported the preparation of various porous materials, such as silica (SiO_2), titania (TiO_2), alumina (Al_2O_3), zirconia (ZrO_2), and yttria (Y_2O_3) particles, using a spray pyrolysis method. This method is promising for the following reasons: it is continuous, rapid, low cost, and the ability to control stoichiometry, size, and compositions is good (Abdullah et al., 2004; Wang et al., 2008). In the spray method, precursors of inorganic salt solutions mixed with colloidal polystyrene latex (PSL), as templates, are often used to prepare porous particles. The porosity and pore size can be easily controlled by changing the PSL contents and sizes, respectively (Iskandar et al., 2001, 2002). The synthesis of other porous particles or films have been extensively investigated by many groups using various methods, such as dip-coating and sol gel methods (Iskandar et al., 2004; Mann et al., 1997). Recent progress in the various methods, available for producing macroporous particles was reviewed by Studart et al. 2006.

However, to the best of our knowledge, few studies have investigated the preparation and characterization of macroporous phosphors, in particular, the rare earth-doped oxide phosphors. In this study, the PL characteristics of macroporous phosphor $\text{Y}_2\text{O}_3:\text{Eu}^{3+}$ particles synthesized using a spray pyrolysis method were investigated. The effects of porosity and particle size on the PL characteristics, including PL intensity, charge transfer peak shift, symmetry ratio, quantum efficiency (QE), and XY CIE chromaticity values were examined in detail.

3.2 Experimental Procedure

The spray pyrolysis experimental setup used in the present study was described in detail in our previous work (Wang et al., 2007a, 2007b). Yttrium nitrate [$\text{Y}(\text{NO}_3)_3 \cdot 6\text{H}_2\text{O}$] and europium nitrate [$\text{Eu}(\text{NO}_3)_3 \cdot 6\text{H}_2\text{O}$] (Kanto Chemical Co., Inc., Tokyo) were used as precursors. and were dissolved in ultrapure water to form

homogeneous aqueous solutions. Europium atoms were added to a doping level of 6 mol% relative to yttrium atoms. To prepare porous yttrium oxide particles, yttrium and europium nitrate aqueous solutions were mixed with 300-nm PSL colloids (Japan Synthetic Rubber Co., Ltd.). The content of the PSL (vol%) added to the precursor, which represents “porosity” in this paper, was calculated based on the volume ratio of PSL/ Y_2O_3 in the final product particles. The precursor solutions were atomized into droplets using an ultrasonic nebulizer (NE-U17, Omron Healthcare Co., Ltd, Tokyo). The mean droplet diameters of the pure yttrium nitrate solution and the mixture of yttrium nitrate and PSL were 5.12 and 5.18 μm , respectively, based on laser diffraction measurements (Spraytec, Malvern Instruments, Ltd., Worcestershire, UK). This result indicates that the presence of PSL colloids in the precursor does not significantly affect the droplet size distribution. The droplets were then carried into a tubular alumina reactor by nitrogen gas at a flow rate of 2 L/min. The tubular reactor was 1 m in length with an inner diameter of 13 mm. The temperatures of five controllable furnace zones were set to 700, 1000, 1400, 1400, and 1400 $^{\circ}\text{C}$. Prior to entering the furnace, the droplets passed through a 20-cm-long zone heated to 160 $^{\circ}\text{C}$ to evaporate water. The resulting particles were collected in an electrostatic precipitator.

The morphology of the synthesized particles was observed using a field emission scanning electronic microscope (FE-SEM, S-5000, Hitachi Corp., Tokyo) operated at 20 kV. The crystallinity was analyzed using X-ray diffraction (XRD, RINT 2200V, Rigaku Denki, Tokyo) with Cu $K\alpha$ radiation in the range of 10-80 $^{\circ}$ at 40 kV and 30 mA. PL properties were examined using a spectrofluorophotometer (RF-5300PC, Shimadzu, Corp., Kyoto) with an excitation wavelength of 254 nm, a bandwidth resolution less than 3 nm, and a signal/noise (S/N) ratio greater than 150. Excitation spectra were recorded under emission at 611 nm using the same equipment. External quantum efficiency (EQE) and CIE chromaticity measurements (C9920-02, Hamamatsu Photonics, Shizuoka) were performed to analyze PL characteristics in detail. All measurements were carried out at room temperature.

3.3 Results and Discussion

To investigate the effect of porosity, particle size was calculated and kept constant based on the typical one droplet to one particle principle (ODOP)(Wang et al., 2007), by changing the concentrations of yttrium and europium nitrate aqueous solutions and corresponding PSL contents from 0.5, 0.3, 0.2, 0.15 to 0.1 M, and 0, 40, 60, 70 to 80 vol%, respectively. On the other hand, to examine the effect of particle size, precursor concentration was altered from 0.0375, 0.1 to 0.15 M with the same PSL content of 80 vol%. The experimental conditions are summarized in detailed in Table 3.1.

3.3.1 Morphology, Particle Size, and Crystallinity Characterization

Figure 3.1 shows FE-SEM images of the particles prepared from precursors with different PSL contents with approximately the same particle size, i.e., 770 nm. Non-porous particles were produced from the precursor without using PSL colloids for comparison. As shown in Fig. 3.1(a), the particles were spherical and dense, as confirmed by computing the particle size based on the one droplet to one particle (ODOP) principle (Wang et al., 2007b). In Fig. 3.1(b), hollow rather than porous particles were generated due to the low PSL contents (40 vol%), which tended to migrate to the center of droplets before decomposition at high temperatures. Increasing the PSL content increased the pore number, as shown in Figs. 3.1(c) and 3.1(d). with addition of 80 vol% PSL to the precursor, pores were seen both inside the particles and also on the particle surface. This result indicates that the PSL particles were well spontaneously well-dispersed during droplet evaporation.

The effect of porous particle size was also investigated by maintaining the constant porosity with addition of 80 vol% PSL colloids to the precursors. Particle size was controlled by varying the concentration of the nitrate solution, i.e., 0.0375, 0.1 to 0.15M, resulting in the average particle sizes of 650, 757, and 886 nm, respectively, as measured from the FE-SEM images shown in Fig. 3.2.

Table 3.1 Effect of porosity and particle sizes on crystallite size, EQE and CIE coordinates.

Sample	C [M]	PSL[vol%]	d_p [nm]	d_c [nm]	EQE [%]	CIE coordinates	
						X	Y
Y-1	0.5	0	757	29.3	60	0.632	0.347
Y-2	0.3	40	757	31.6	74	0.642	0.343
Y-3	0.2	60	757	31.6	76	0.642	0.342
Y-4	0.15	70	757	31.6	77	0.642	0.342
Y-5	0.1	80	757	30.4	79	0.641	0.341
Y-6	0.0375	80	650	29.3	65	0.642	0.340
Y-7	0.15	80	886	34.2	80	0.641	0.340

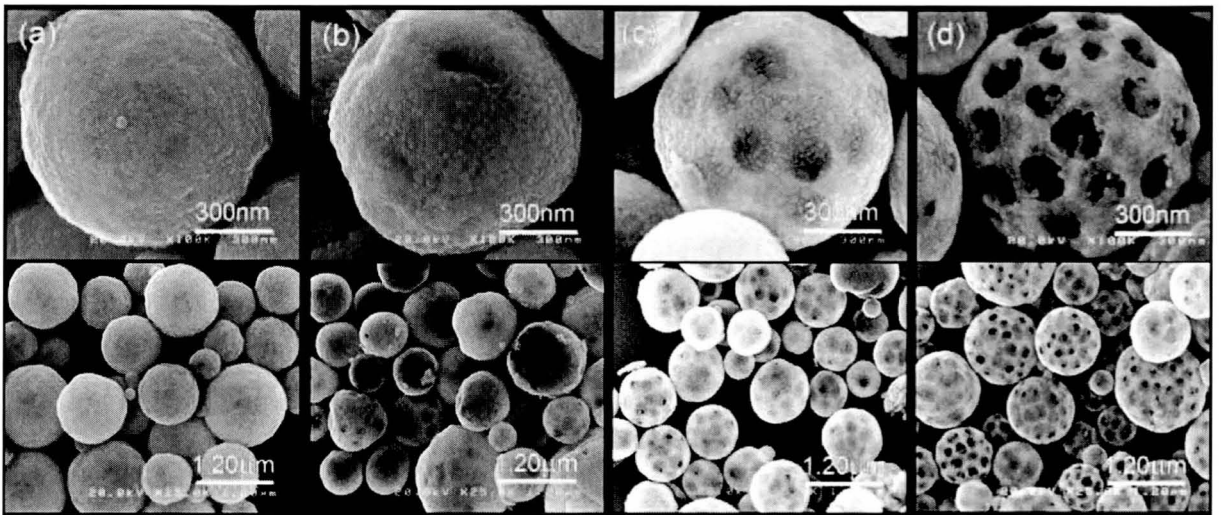


Fig. 3.1 FE-SEM images of particles prepared from precursors with PSL contents of (a) 0, (b) 40, (c) 60, and (d) 80 vol%.

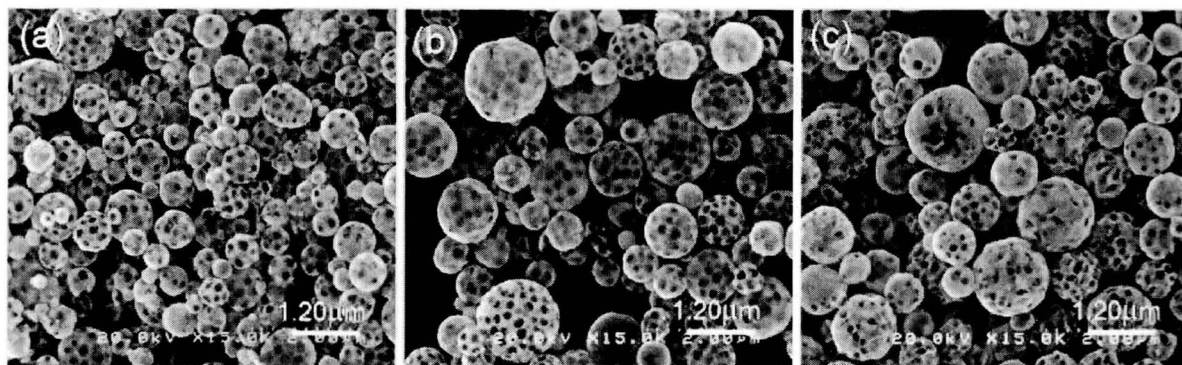


Fig. 3.2 FE-SEM images of particles prepared from precursors with different concentrations of 80 vol% PSL (a) 0.0376, (b) 0.1 and (c) 0.15 M.

XRD patterns of the generated particles are presented in Fig. 3.3. All particles were characterized as pure body centered cubic (bcc) Y_2O_3 phase corresponding to JCPDS No. 41-1105 with no impurities nor phase transition. In addition, clear peaks were observed for all particles, indicating that the selected furnace temperature profile was effective for the synthesis of both dense and porous particles with relatively high crystallinity. The crystallite sizes were calculated using the Scherrer equation based on full width at half maximum (FWHM) values at $2\theta = 29.1^\circ$. The crystallite size was 29.3 nm for non-porous particles. For most porous particles that were similarly sized as non-porous particles, crystallite size was relatively constant at approximately 31.6 nm. For porous particles with higher porosity synthesized from precursor with 80 vol% PSL contents, the crystallite size declined slightly to approximately 30.4 nm. The slightly higher crystallinity in porous particles might be due to the relatively lower inorganic salt content in the precursor under the same heat treatment. However, in the case of particles with high porosity, more energy is required for evaporation/decomposition of the PSL particles (e.g. 80 vol%), resulting in a decrease in crystallite size. The crystallite size of different sized particles was also shown by the XRD patterns in Fig. 3.3. It is evident that increasing particle sizes from 650 to 886 nm by increasing the precursor concentrations from 0.0375 to 0.15M with the same heat treatment leads to an increase in crystallite sizes from 29.3 to 34.2 nm. This phenomenon occurs because crystallite growth is affected by the number concentration of Y_2O_3 primary particles (nuclei) and the solvent concentration that must be evaporated. At equivalent droplet energy, the nucleation occurs earlier for more concentrated precursors, consequently the time available for crystal growth is longer, resulting in higher crystallinity. Another reason that particles prepared from less concentrated precursors is that less energy is available for crystal growth, as more energy is needed for solvent evaporation.

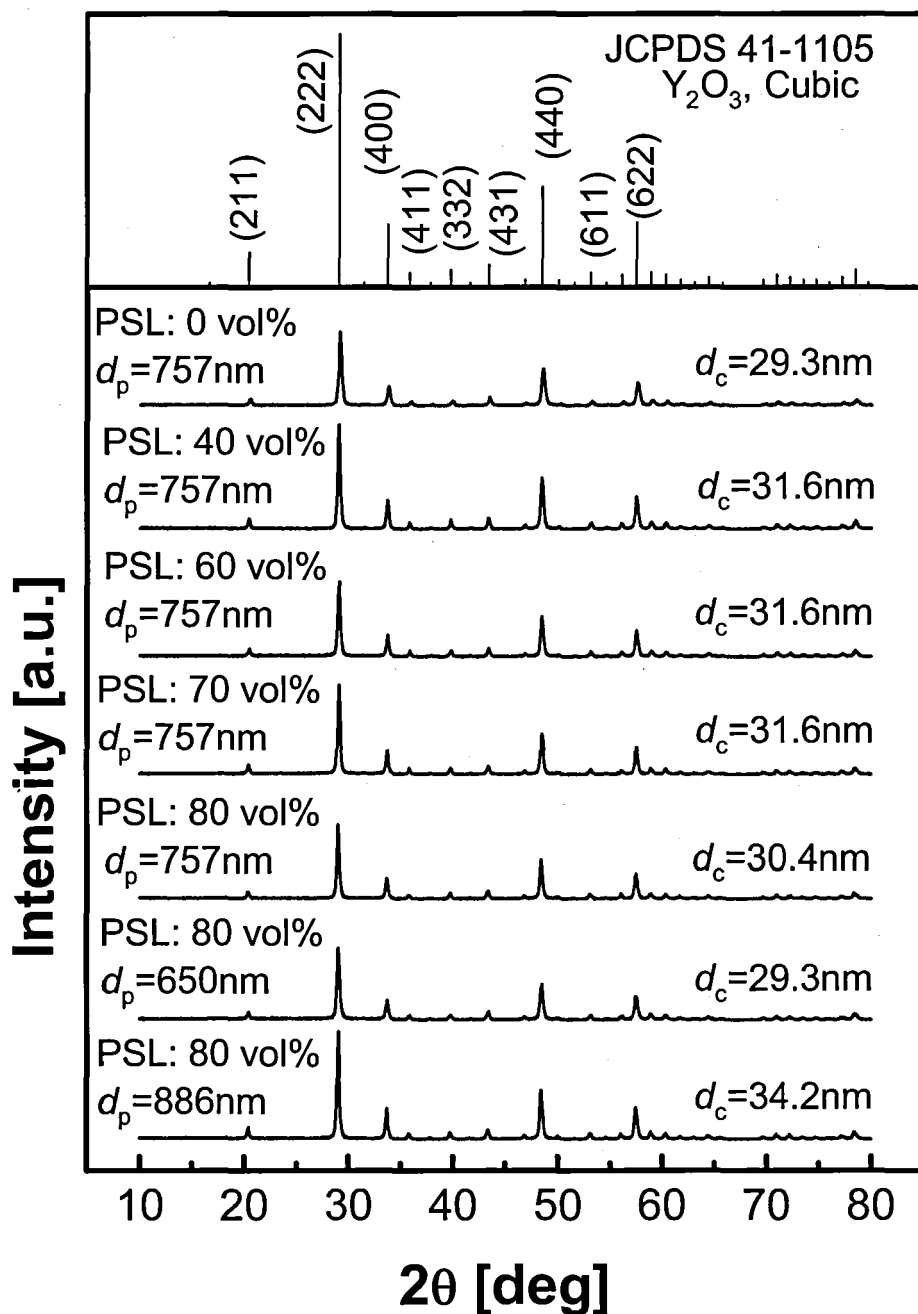


Fig. 3.3 XRD patterns of particles with different porosities and particle sizes.

3.3.2 Photoluminescence Spectra

Figure 3.4 shows PL emission spectra of $\text{Y}_2\text{O}_3:\text{Eu}^{3+}$ particles with different porosities (i.e., different PSL contents) (a) and particle sizes (b). A strong emission peak at 611 nm in PL emission spectra is due to 5D_0 to 7F_2 allowed electrical dipole transition of Eu^{3+} . The intensity of the main emission peak increases with increasing porosity, i.e., PSL contents. The relative PL intensity of the strongest emission peak at 611 nm and crystallite size as a function of porosity is shown in Fig. 3.5(a). The PL intensity of non-porous particles was assumed as the base (100%) for comparison. As shown in the figure, the relative PL intensity increased significantly from non-porous particles to porous particles with addition of 40 vol% PSL. The relative PL intensity for porous particles continued to increase to 133% that of non-porous particles with addition of 70 vol%. In the case of porous particles with addition 80 vol% PSL, approximately 135% relative PL intensity was achieved. The crystallite size also tends to increase with increasing the porosity and then it maintains a relatively constant value for 40-70 vol% PSL in the precursor. The crystallite size decreases for porous particle that were synthesized using >70 vol% PSL in the precursor, as explained above.

Based on the results of the present study, it is obvious that the crystallinity is not the main reason for the greater PL intensities of the porous particles. Therefore, the primary explanation for the phenomenon is their porous structures. The Y_2O_3 base crystal has two symmetry types, C_2 and C_{3i} . The PL emission peaks at 587.7 nm [${}^5D_0(C_2) \rightarrow {}^7F_{1a}(C_2)$] and 582.4 nm [${}^5D_0(C_{3i}) \rightarrow {}^7F_{1a}(C_{3i})$] were transformed from C_2 and C_{3i} states, respectively shown in Fig. 3.4(c). The ratio of the PL emission peak intensity at 587.7 nm to that at 582.4 nm is defined as the symmetry ratio of C_2 to C_{3i} sub-lattices, which is the basic parameter by which PL emission spectra are evaluated. As stated in our previous paper, a symmetry ratio of approximately 3 indicates that Eu^{3+} does not preferentially occupy the C_2 and C_{3i} sites (Minami et al., 2008). Porous particles exhibit lower symmetry than non-porous particles. For example, the symmetry ratios were calculated to be 2.7 and 3.1 for porous particles with 80 vol% PSL addition and non-porous particles of the same particle size, respectively. Compared with non-porous particles, porous particles have more atoms located on the particle surface due to their

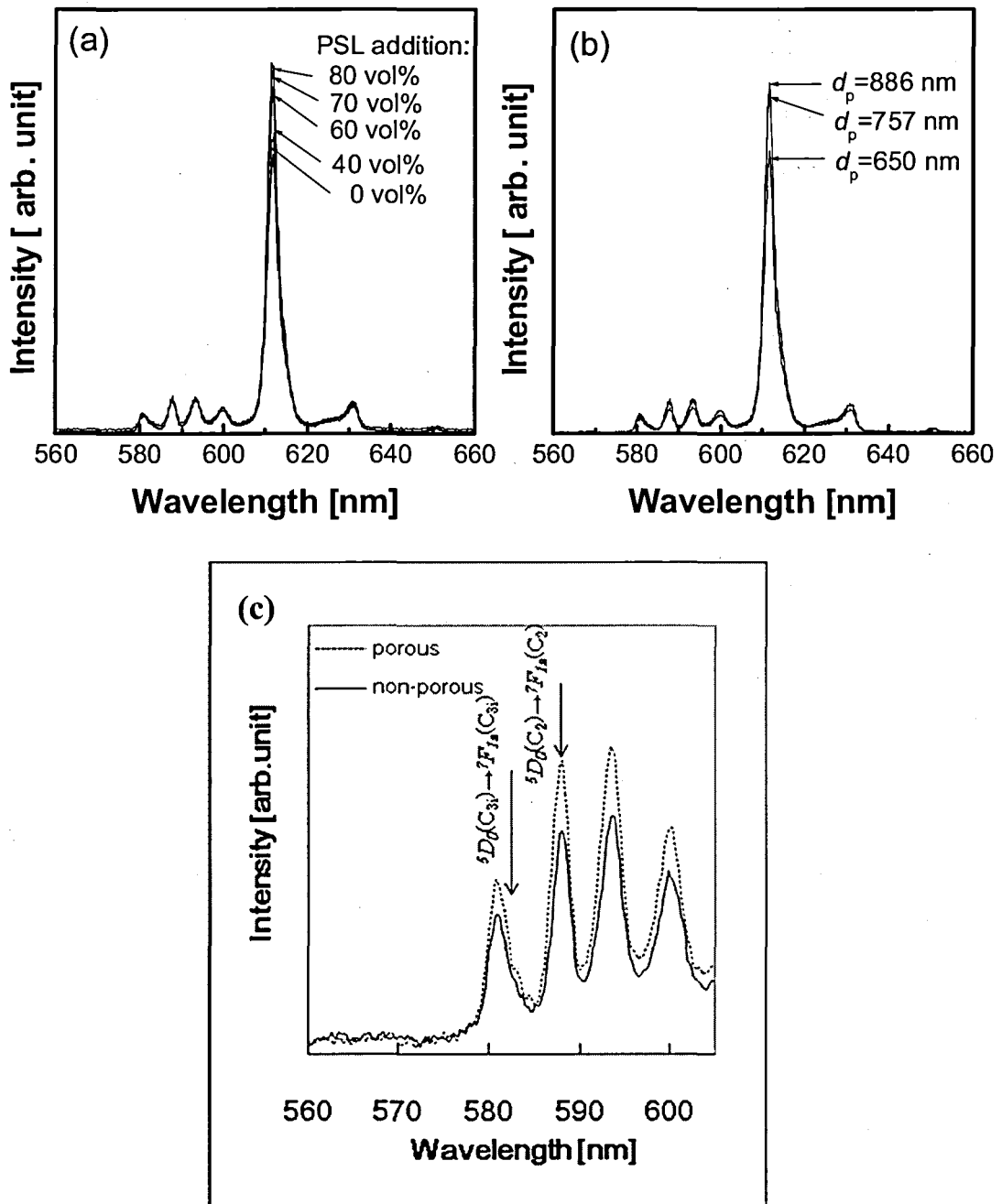


Fig. 3.4 PL emission spectra of $\text{Y}_2\text{O}_3:\text{Eu}^{3+}$ particles as functions of (a) porosity plotted against volume percentages of added PSL and (b) particle size with a constant PSL content of 80 vol%; and (c) magnified PL spectra from 570 to 600 nm for both porous (80 vol%) and non-porous particles.

high surface area, and the surface defects in the crystallites may occur more frequently. Porous particles showed as a character of small crystallite size of non-porous particles, if the crystallite size and particles size of both of them are same. These defects may increase the degree of disorder and lower the local symmetry of Eu^{3+} ions located near the surface. The reduced local symmetry, in other words, the increased a symmetry, will lead to differences in the intensity ratio of $\text{Y}_2\text{O}_3:\text{Eu}^{3+}$ phosphor particles, and hence the increase of PL emission intensity (Wang et.al.(2007)a, Minami et.al.)

Figure 3.5(b) shows very similar PL emission spectra of $\text{Y}_2\text{O}_3:\text{Eu}^{3+}$ porous particles with different particle diameters. The PL emission intensity increases significantly when the particle size was increased from 650 to 757 nm, but remained constant for particles larger than 800 nm [Fig. 3.5(b)]. This phenomenon was also observed and explained by our previous investigation for non-porous $\text{Y}_2\text{O}_3:\text{Eu}^{3+}$ particles (Wang et al., 2007a).

To further investigate the PL characteristics of the porous particles, the excitation spectra were also recorded for particles with different porosities and particle sizes (Figure 3.6(a) and 3.6 (b), respectively). The broad excitation spectrum peak located at around 250 nm in Fig. 3.7(a) was assigned to the excited charge-transfer band (CTB) of Eu^{3+} . The CTB peak wavelength of the non-porous particles locates at 250 nm, which is the same value as that of the bulk. CTB peak wavelengths of the porous particles with addition of 40, 60, 70, and 80 vol% PSL were blue-shifted from 248, 247, 246 to 246 nm, respectively. In our previous report (Minami et al., 2008), $\text{Y}_2\text{O}_3:\text{Eu}^{3+}$ particles has blue shifted CTB peak proportional to the diameter of the particles less than 600 nm. Results of our previous study revealed that the CTB peak wavelengths of $\text{Y}_2\text{O}_3:\text{Eu}^{3+}$ 590-nm and 390-nm non-porous particles were 247, and 244 nm, respectively (Minami et al., 2008). As shown in Fig. 3.6(b), the porous particles with an average size of 770 nm (with addition of 60 and 70 vol% PSL) show approximately the same CTB wavelength as the 590-nm non-porous particles. Van Pieterse et al. 2000 reported that the peak wavelength shift of the CTB by different host crystals, such as Y_2O_3 , $\text{Y}_2\text{O}_2\text{S}$, and YPO_3 , is determined by the nature of the ligand, the metal ion, the coordination, and the size of cation site (van Pieterse et al., 2000). In $\text{Y}_2\text{O}_3:\text{Eu}^{3+}$, the CTB is closely related to the covalency between O^{2-} and Eu^{3+} and the coordination environment Eu^{3+} .

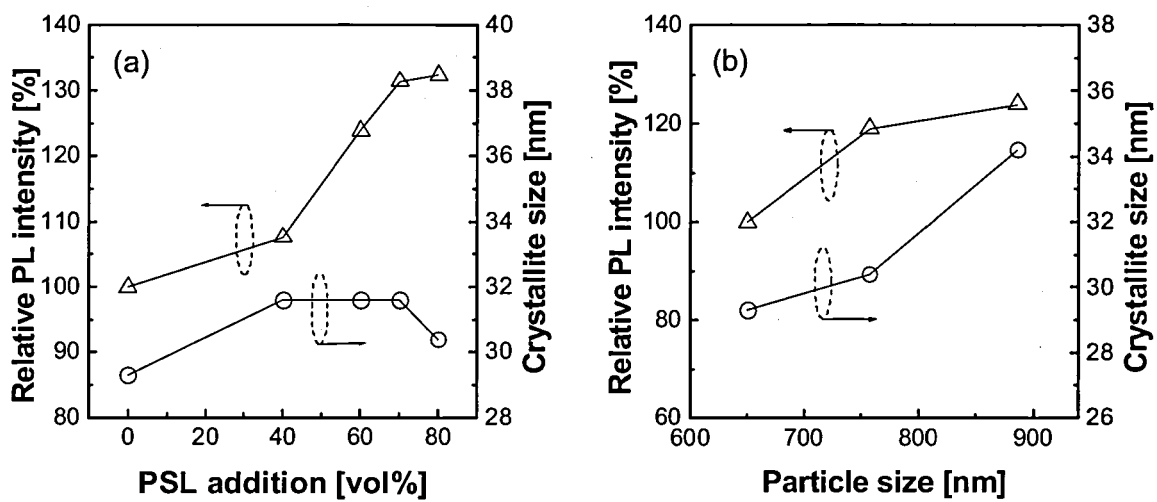


Fig. 3.5 PL excitation spectra of $Y_2O_3:Eu^{3+}$ particles as functions of (a) porosity and (b) particle size.

The Eu-O distance is the primary determinant of the CTB peak position. Crystallite size has a minor influence, and particle size has major influence, on the CTB peak shift (Minami et al., 2008). For porous particles, the blue-shift was due to the bond length of Eu-O and its covalency. For porous particles, the porous structure may be the primary determinant of the coordination environment of Eu^{3+} and, hence, the Eu-O bond distance. Therefore, porous particles show a CTB blue-shift. In Fig. 3.6(b), the PL excitation peak was maintained at approximately 246 nm, indicating that CTB did not change with particle size in this region.

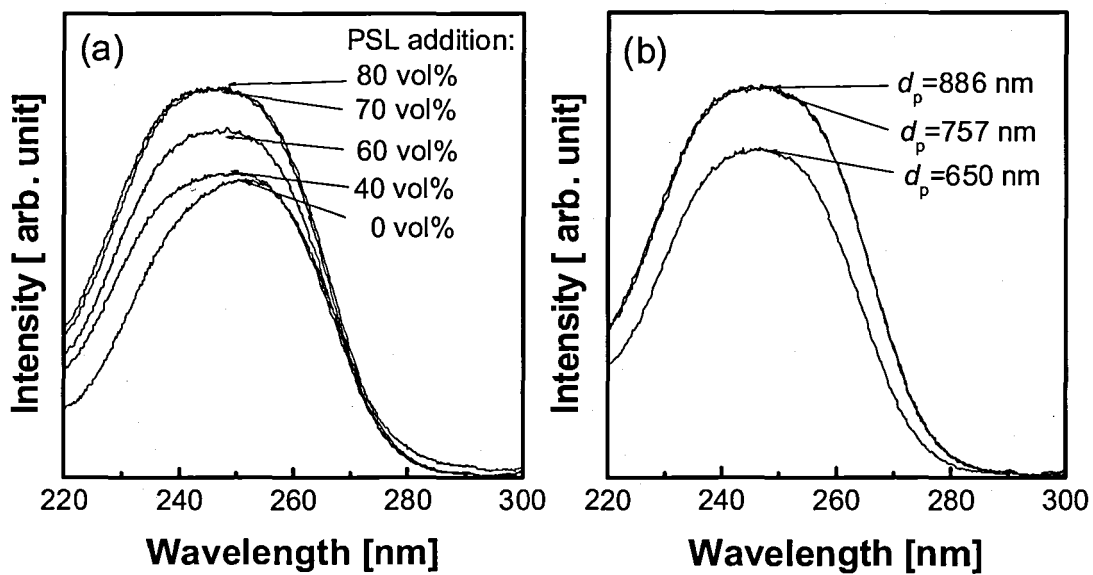


Fig. 3.6 Relative PL emission peak intensity and crystallite size of the generated particles as functions of (a) porosity and (b) particle size.

3.3.3 Color Rendering Properties

The effects of porosity and particle size were also examined using EQE measurements. The EQE values of all samples are listed in Table 1. The EQE values increase with increasing porosity. For example, the EQE value of non-porous particles increases significantly from 60 to 74% for the particles synthesized using addition of 40 vol% PSL to the precursor. The EQE value reached 79% for particles synthesized using addition of 80 vol% PSL. In the case of particle EQE measurements confirmed the PL intensity measurements.

The CIE1931 XY chromaticity coordinate graph was plotted to characterize the color rendering properties of the samples, as shown in Fig. 3.7. The CIE chromaticity coordinates of saturated red phosphors based on the standard of National Television Standard Committee (NTSC) is at $x = 0.67$ and $y = 0.33$ (Niu et al., 2005). As shown in Table 1, the chromaticity coordinates of all samples were very close to the standard x value, indicating that high quality red-emitting phosphor particles, efficient for most applications, were generated. Moreover, the quality the red, ordered macroporous particles were slightly superior to that of non-porous particles, even if the mass density of the macroporous particles was reduced due to high porosity.

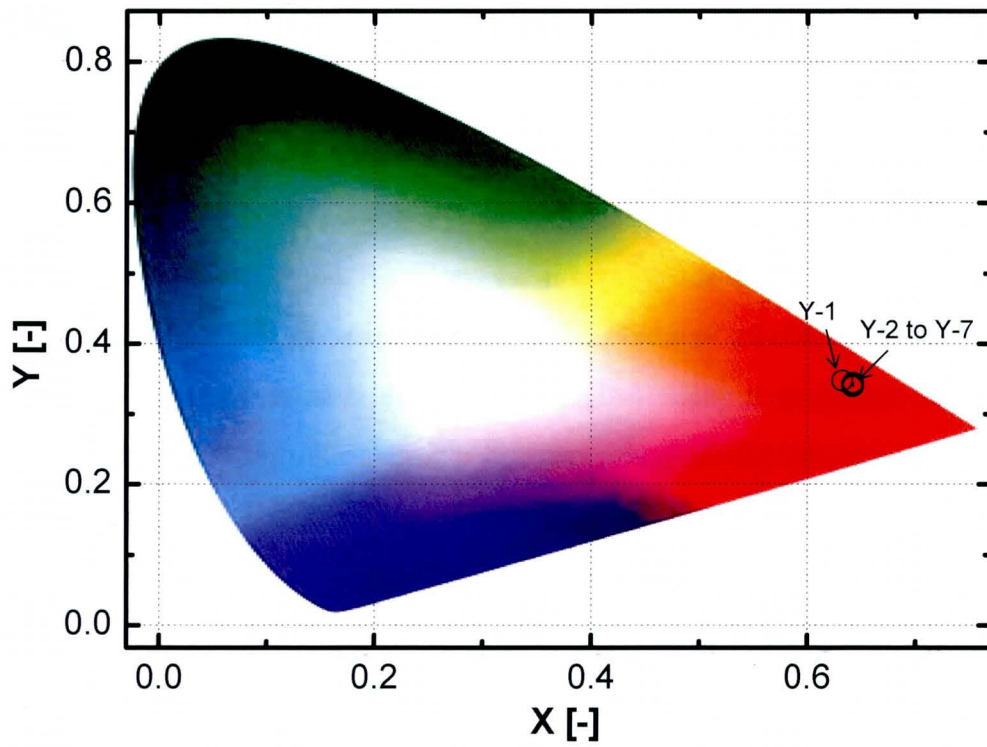


Fig. 3.7 CIE chromaticity diagram of $\text{Y}_2\text{O}_3:\text{Eu}^{3+}$ particles with different porosities and particles sizes (samples of Y-1 to Y-7) as indicated in Table 3.1.

3.4 Summary

Ordered macroporous, red-phosphor particles with high quantum efficiency and sharp red-emission indicated by XY CIE chromaticity were synthesized by spray pyrolysis. The Porous particles had unique photophysical properties, such as a 4-nm blue-shift of CTB wavelength, and a lower symmetry ratio of 2.7, that were not shown by non-porous particles with approximately the same particle and crystallite sizes. The structure of these porous particles is considered the main reason for the phenomena. These results suggest that the porous phosphor particles are promising for a variety of applications in advanced industries due to their high PL characteristics, low density, and hierarchical structures.

References

- Abdullah, M., F. Iskandar, S. Shibamoto, T. Ogi and K. Okuyama, "Preparation of oxide particles with ordered macroporous by colloidal templating and spray pyrolysis", *Acta Mater.* 52 (2004) 5151-5156
- Iskandar, F., Mikrajuddin and K. Okuyama, "In situ production of spherical silica particles containing self-organized mesopores", *Nano Lett.*, 1 (2001) 231-234
- Iskandar, F., Mikrajuddin, and K. Okuyama, "Controllability of pore size and porosity on self-organized porous silica particles", *Nano Lett.*, 2(2002) 389-392
- Iskandar, F., M. Abdullah, H. Yoden, K. Okuyama, "Silica films containing ordered pores prepared by dip coating of silica nanoparticles and polystyrene beads colloidal mixture", *J. Sol-Gel Sci. Technol.*, 29 (2004) 41-47
- Joffin, N., J. Dexpert-Ghys, M. Verelst, G. Baret, and A. Garcia, "The influence of microstructure on luminescent properties of $Y_2O_3:Eu$ prepared by spray pyrolysis", *J. Lumin.* 113 (2005) 249-257
- Jones, S. L., D. Kumar, R. K. Singh, and P. H. Holloway, "Luminescence of pulsed laser deposited Eu doped yttrium oxide films", *Appl. Phys. Lett.* 71 (1997) 404-406
- Liu, G., and G. Hong: *J. Nanosci. Nanotechnol.* 6 (2006) 120-124.
- Mann, S., S. L. Burkett, S. A. Davis, C. E. Fowler, N. H. Mendelson, S. D. Sims, D. Walsh, and N. T. Whilton, "Sol-gel synthesis of organized matter", *Chem. Mater.* 9 (1997) 2300-2310
- Minami, T., W-N. Wang, F. Iskandar, and K. Okuyama, "Photoluminescence properties of submicrometer phosphors with different crystallite/particle sizes", *Jpn. J. Appl. Phys.* 47 (2008) 7220-7223
- Niu, Y. -H. , Y.-L. Tung, Y. Chi, C.-F. Shu, J. H. Kim, B. Chen, J. Luo, A. J. Carty, and A. K.-Y. Jen, "Highly efficient electrophosphorescent devices with saturated red emission from a neutral osmium complex", *Chem. Mater.* 17 (2005) 3532-2536
- Okuyama, K., M. Abdullah, I. W. Lenggoro and F. Iskandar, "Preparation of functional nanostructured particles by spray drying-a review", *Adv. Powder Technol.*, 17 (2006) 587-611

- Shea, L. E., J. Mckittrick, M. L. F. Phillips, "Predicting and modeling the low-voltage cathodoluminescent efficiency of oxide phosphors", *J. Electrochem. Soc.* 145 (1998) 3165-3170
- Studart, A. R., U. T. Gonzenbach, E. Tervoort, L. J. Gauckler, "Processing routes to macroporous ceramics:a review", *J. Am. Ceram. Soc.* 89 (2006) 1771-1789
- Wang, F., R. Liu, A. Pan, S. Xie and B. Zou, "A simple and cheap way to produce porous ZnO ribbons and their photovoltaic response", *Mater. Lett.* 61 (2007) 4459-4462
- Wang, H. Q. , G. Z. Wang, L. C. Jia, C. J. Tang, and G. H. Lie, "Polychromatic visible photoluminescence in porous ZnO nanotubes", *J. Phys. D: Appl. Phys.* 40 (2007) 6549-6553
- Wang, W-N., W. Widiyastuti, T. Ogi, I. W. Lenggoro, and K. Okuyama, "Correlations between Crystallite/Particle Size and Photoluminescence Properties of Submicrometer Phosphors", *Chem. Mater.* 19 (2007a) 1723-1730
- Wang, W-N., W. Widiyastuti, I. W. Lenggoro, T. O. Kim, and K. Okuyama, "Photoluminescence optimization of luminescent nanocomposites by spray pyrolysis of a colloid-solution precursor", *J. Electrochem. Soc.* 154 (2007) J121-J128
- Wang, W-N., F. Iskandar, K. Okuyama, and Y. Shinomiya, "Rapid synthesis of non-aggregated fine chlorapatite blue phosphor powders with high quantum efficiency", *Adv. Mater.* 20 (2008) 3422-3426
- van Pieterse, L., M. Heeroma, E. de Heer, and A. Meijerink, "Charge transfer luminescence of Yb³⁺", *J. Lumin.* ,91 (2000) 177-193
- Yan, H., Y. Yang, Z. Fu, B. Yang, Z. Wang, L. Xia, S. Yu, S. Fu, and F. Li, "Fabrication of 2D ordered porous ZnO films using 3D opal templates by electrodeposition", *Chem. Lett.* 34 (2005) 976-977
- Yang, P., S. Huang, D. Kong , J. Lin, and H. Fu, "Luminescence functionalization of SBA-15 by YVO₄:Eu³⁺ as a novel drug delivery system", *Inorg. Chem.* 46 (2007) 3203-3211

Chapter 4

Chemical and Photoluminescence Analysis of New Carbon-based Boron Oxynitride Phosphor Particles

4.1 Introduction

Much effort has been devoted to the development of carbon-based luminescent materials, such as carbon-based boron nitride (BCN) for use as phosphors. These investigations begin with BN materials. BN is an insulator that has several kinds of conformation, such as h-BN, t-BN (Guo et al., 2005), r-BN, c-BN, and w-BN. Several methods have been applied for synthesis of BCN materials. The resulting BCN materials revealed some luminescence properties (Kawaguchi, 1997). For example, BCN nanotubes were investigated as a tunable luminescent material having wavelengths from 370 nm to 470 nm (Bai et al., 2000), B₃CN₃ fibers also exhibited two photoluminescence (PL) peaks at 370 nm and 700 nm (Yang et al., 2006). However, the PL intensity and quantum efficiency (QE) of the BCN phosphors remained very low (reported QE < 0.5%) (Chen et al., 1999). Further, the BCN phosphors were generally prepared under severe conditions, such as high pressure and high temperature (Hubert et al., 1997).

Therefore, the development of a facile method for the preparation of carbon-based phosphors is essential. We recently reported on the successful preparation of carbon-based oxynitride, i.e., BCNO phosphor powders using a one-step liquid process at relatively low temperature (below 900 °C) under ambient atmospheric conditions. The prepared powders exhibited tunable photoluminescence spectra from violet to

near-red regions and possessed high external QE (Ogi et al., 2008). However, detailed characterization of the BCNO phosphors has not been developed. In this thesis, I report further analysis of chemical configuration and PL properties including QE of the BCNO phosphors. A possible formation mechanism of BCNO phosphors was proposed as well.

4.2 Experimental Procedure

The BCNO phosphors were synthesized from the following precursors: boric acid (H_3BO_3), as the boron source; urea ($(\text{NH}_2)_2\text{CO}$), as the nitrogen source; and, polyethylene glycol (PEG), $\text{H}(\text{OEG})_n\text{OH}$, with $M_w = 20,000$ and $\text{EG} = \text{OCH}_2\text{CH}_2$, as the carbon source. All chemicals were purchased from Wako Chemicals Co., Ltd., Japan, and were used without further purification. The precursors were mixed in pure water and the resulting solution was heated at 700-900 °C for 30-60 min to obtain BCNO particles. The detailed explanations were described in the previous paper (Ogi et al., 2008).

The chemical composition of the prepared phosphors was characterized using an electron energy-loss spectrometer (EELS) with transmission electron microscopy (TEM, JEM-3000F, JEOL, Tokyo, Japan) at 300 kV. EELS involves the measurement of the energy imparted to a thin (= 200 nm) specimen by fast (= 100 keV) incident electrons, and is well adapted to light-element analysis, from which high spatial resolution of chemical information can be gained (Brydson et al., 1991; Keast et al., 2001; Garvie et al., 1999). The PL spectra were recorded at room temperature by means of a spectrofluorophotometer (RF-5300PC, Shimadzu Corp., Kyoto, Japan) equipped with a xenon lamp source. The external quantum efficiency was analyzed using an absolute PL quantum yield measurement system (C9920-02, Hamamatsu Photonics, Shizuoka, Japan). All PL analyses were performed at an excitation wavelength of 365 nm.

4.3. Results and Discussion

4.3.1 Chemical Analysis

Representative EELS spectra of the resulting BCNO phosphors, which were prepared at 800 °C for 30 min, are shown in Fig. 4.1. Four ionization edges of B, C, N and O are indicated in a low-resolution spectrum (Fig. 4.1(a)). Each atom has at least two ionization peaks in its corresponding spectrum, with lower energy is typically assigned to π^* bonds and the higher belonging to σ^* bonds, since the former (i.e., π^* bonds) is generally weaker than the latter (i.e., σ^* bonds) according to the classical valence bond theory (McMurry et al., 2001).

Figure 4.1 (b) shows two sharp peaks of B-K ionization at 193 and 201 eV for π^* and σ^* electrons, respectively. As Garvie et al. (1999) reported, in the case of a BCNO compound, if the B-K ionization for π^* electrons has three peaks of 189.3, 192.1, and 194.1 eV, the B atom is surrounded by three elements, i.e. three Cs, three Ns, and three Os, respectively. From our results, since the B-K ionization for π^* electrons has only one peak between 192 and 194 eV, it means that the B atom is intermediately surrounded by Ns and Os atoms, which also implies that there are no clear B-C chemical bonds in the BCNO particles.

Figure 4.1(c) presents the spectrum of the C-K ionization edges. The peak at 285 eV is assigned to π^* bands, while those at 288 and 295 eV are assigned to σ^* bands, in which the peak at 288 eV has C-H* features (Keast et al. 2001). Previous research showed that materials with weak sp^2 hybrid orbitals, such as amorphous carbon, graphite, and solid benzene, can have a π^* feature; while those having stronger sp^3 hybridization (McMurry et al. 2001), such as a diamond and solid cyclohexane, exhibit only σ^* (including C-H*) features with no π^* bands. The C-H* feature can usually be found in organic materials, such as solid benzene and cyclohexane (Keast et al., 2001; Garvie et al., 1999). In the present study, the C-H bonds are supposed to come from the organic residue of decomposed PEG. Since these data are evidence that the C atoms in the BCNO phosphors have π and σ bonds, they should have sp^2 hybridization (McMurry et al., 2001). The sp^2 hybrids lie in a plane and are oriented toward the corners of an

equilateral triangle at angles of 120° to one another and have a framework

consisting mainly of a 6-membered carbon ring (McMurry et al. 2001). Previously reported EELS data (Keast et al., 2001; Garvie et al., 1999) of C-K edges from different carbon sources supported the above hypothesis that the carbon in the BCNO compound has an amorphous structure with traces of C-H groups (organic residue). They should not have a sp^3 structure that is rigid and hard, which can be obtained only under severe conditions (Hubert et al., 1997) In the present study, the BCNO compounds were prepared at low temperature (below 900°C) and under ambient atmospheric conditions, resulting in powder with a soft framework (sp^2 hybridization).

Figure 4.1(d) shows the ionization peak of N for π^* character at 403.5 eV and σ^* character at 410.5 eV. Since σ^* peak intensity of N is higher than that of π^* peak, this means that the major of the N atoms have σ^* bonds with other elements. The ionization peak spectrum of O is shown in Fig. 4.1(e), where the peak at 537 eV is for π^* character and 545 eV is for σ^* . The results indicate that the N and O atoms are chemically bonded with B atoms in the BCNO phosphors.

A comparison of the shapes of B, C, N, and O K edges was made as shown in Fig.4.2. Each EELS spectrum of B, C, N and O was shifted by setting their corresponding rising edges of K ionization spectra at 0 eV (Keast et al., 2001). The shapes and positions of B, N, and O are almost the same at the relative energy loss of around 3 eV and 10 eV, suggesting a similar bonding environment (π^* and σ^* characters) and covalency of each element. The shape of C-K edges is distinct due to presence of amorphous and organic carbon. From these EELS spectra, we can thus conclude that the prepared BCNO powder has covalently bonded B, N, and O atoms with soft (sp^2 hybridization) carbon framework.

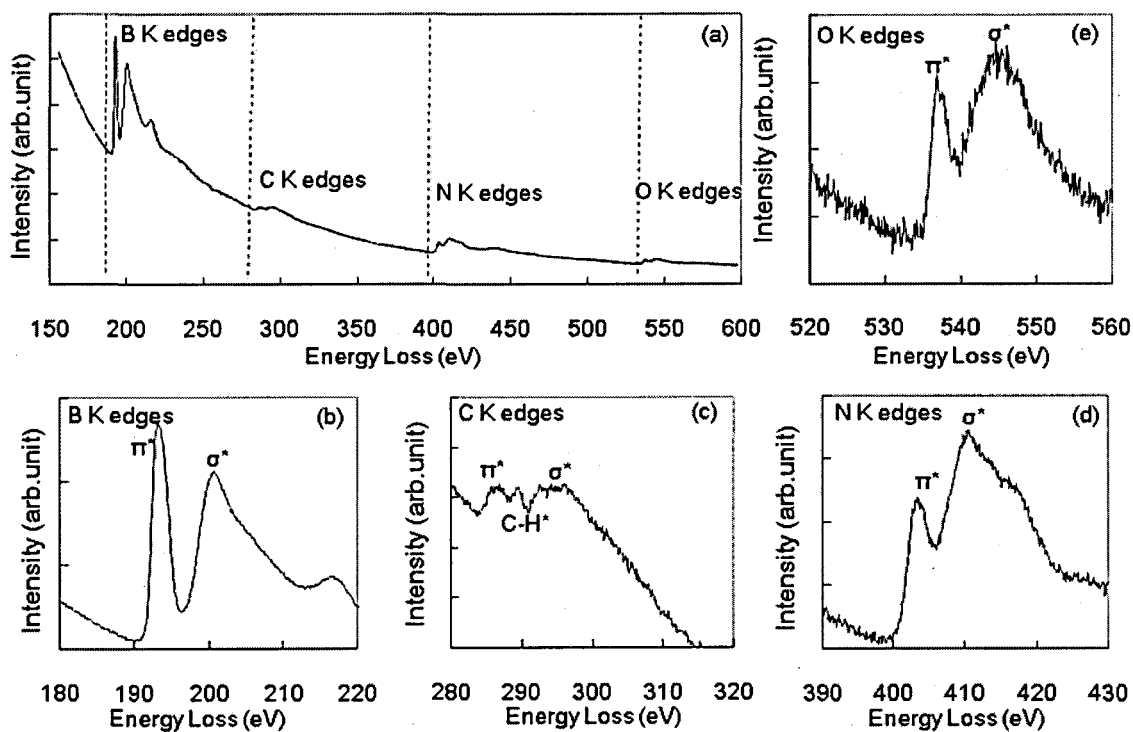


Fig. 4.1 Representative electron energy loss spectra of BCNO phosphors prepared at 800 °C for 30 min with PEG/B = 2×10^{-3} (mol/mol). (a) total spectrum, (b) ionization edges of Boron, (c) ionization edges of Carbon, (d) ionization edges of Nitrogen, and (e) ionization edges of Oxygen.

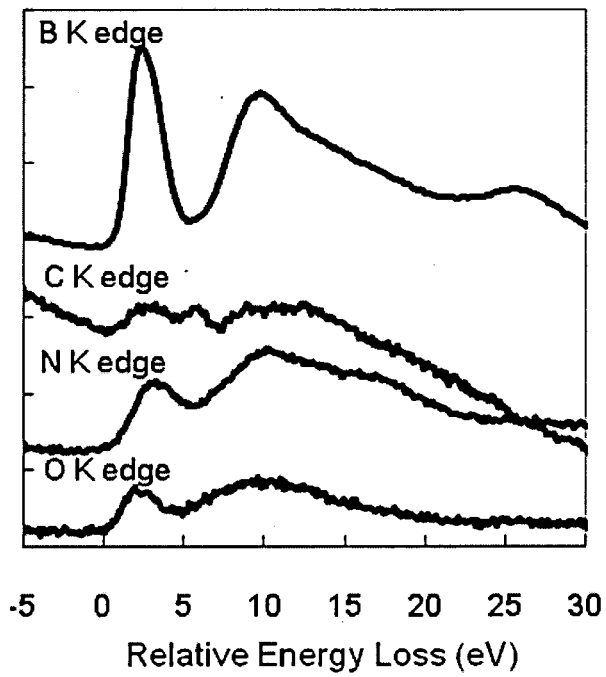


Fig. 4.2 Relative energy loss spectra of K edges of BCNO phosphor. All spectra on a common energy scale and shifted to align relative to their signal of Electron energy loss spectroscopy. Dotted line is indicating relative energy loss of 2 and 10 eV.

4.3.2 Photoluminescence Characterization

In addition to the above chemical analysis, a detailed PL characterization of the prepared BCNO phosphors was carried out. Figure 4.3 shows the PL emission spectra and the figures of the corresponding emission peak wavelength as well as the quantum efficiency of the BCNO phosphor particles as a function of the synthesis temperature. Several PL peak wavelength has a linear relationship with the process temperature – they blue-shifted from 485 nm to 387 nm as the process temperatures increased from 700 to 900 °C. From these results, we find that the maximum QE of 79% was obtained at 800 °C with a PL peak wavelength at around 470 nm. The effect of heating time was investigated as well (Fig.4.4). Similar results, that is, blue shift of PL wavelength peak and enhanced quantum efficiency were obtained as heating time increased from 30 to 60 min.

The above phenomena can be explained by a possible BCNO formation mechanism as follows. The precursors, i.e., boric acid, PEG and urea, first react to form a BCNO compound in a hexagonal structure with water as a byproduct. In the case of low energy input, i.e. low heating temperature (e.g. 700 °C) or short heating time (e.g. 30 min), the chemical reaction for BCNO formation is incomplete. Subsequently, the resulting phosphors have hydroxyl groups on the surface. Due to the presence of the excess OH groups, the partially formed BCNO has fewer free electrons to share in the total molecule compared with completely formed BCNO. Thus, the bond strength and length of partially formed BCNO is weaker and longer, respectively, than that of completely formed BCNO. This means the energy gap of partially formed BCNO also is lower than that of complete BCNO, which is the main reason for the PL red shift of partially formed BCNO. After an increase of input energy, the OH groups are removed, which results in a relatively pure BCNO compound with a hexagonal framework. A Further increase in the input energy, for example, 900 °C, results in a BCN phosphor by releasing O, and, finally, BC_xN or BN will be formed. Our very recent results also confirmed that BCNO formed at 900 °C has no B-O bonds from their FT-IR spectra (Kaihatsu et. al. 2009).

Since the resulting BCNO compounds show a very high QE, it can be inferred that they are, at least partially, direct bandgap phosphors. In semiconductor physics, a direct bandgap means that the minimum energy of the conduction band lies directly above the maximum energy of the valence band in momentum space. A direct bandgap phosphor always has very high PL properties (Nara et al. 2006, Neamen 2003). For the present study, we assumed that the atomic distances of BCNO were relatively shorter than those of BC₂N, because O has a higher electron affinity and has a smaller covalent bond radius than those of B, C or N atoms. Since the atomic distance is shorter, the valence band and the conduction band shifted closer. Accordingly, the energy difference between them becomes larger. The small difference in atomic distance makes a direct bandgap character and the larger energy difference creates a blue shift for BCNO phosphor.

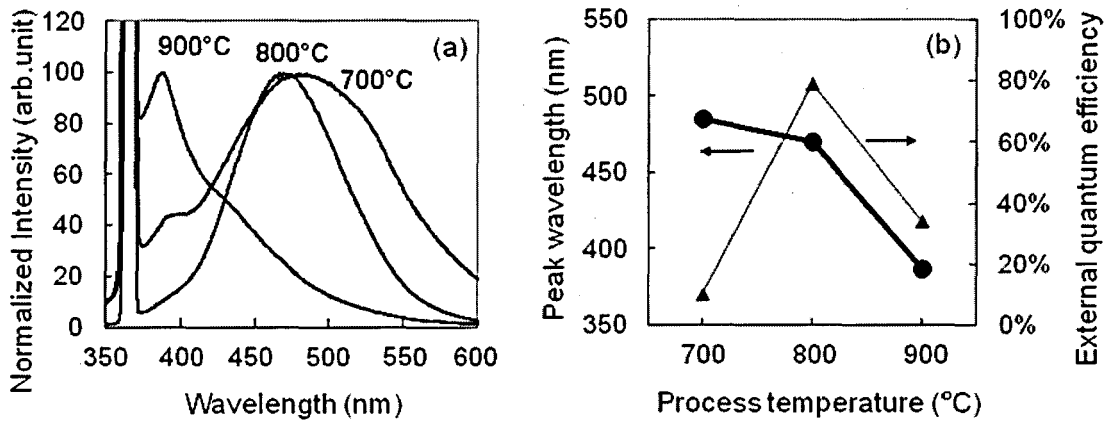


Fig. 4.3 Photoluminescence spectra of phosphor particles with different sample preparation. (a) PL spectrum of phosphor particles and (b) PL Peak wavelength (circle) and its quantum efficiency (triangle) of phosphor particles, prepared by processing temperature at 700, 800 and 900 °C for 30 min and prepared using PEG/B = 2.0×10^{-3} (mol/mol)

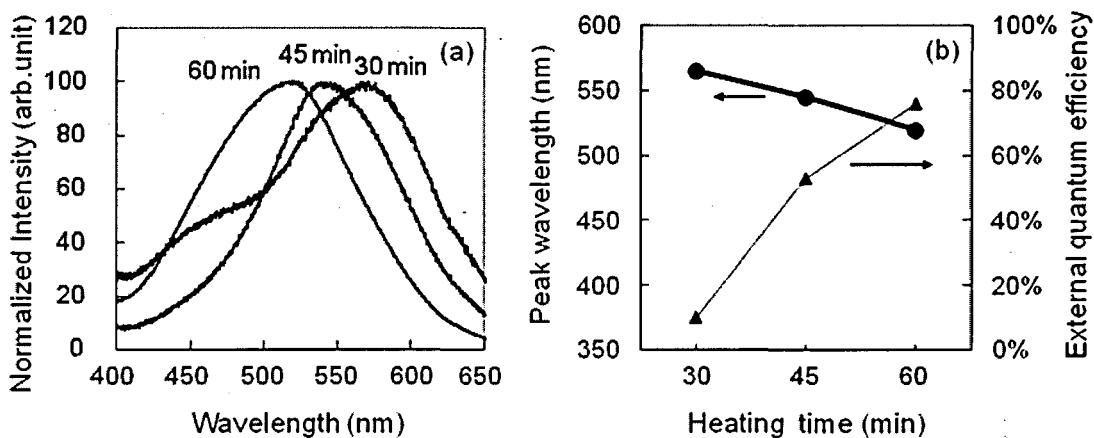


Fig. 4.4 Photoluminescence spectra of phosphor particles with different sample preparation. (a) PL spectrum of phosphor particles and (b) PL Peak wavelength (circle) and its quantum efficiency (triangle) of phosphor particles, prepared by heating time at 30, 45, and 60 min for 700 °C, and prepared using PEG/B = 4.0×10^{-3} (mol/mol) for 60 min and 45 min, PEG/B = 4.4×10^{-3} (mol/mol) for 30 min.

4.4 Summary

4. Conclusions

The chemical and PL properties of BCNO phosphor particles were investigated. The EELS results showed that the prepared BCNO has covalently bonded B, N, and O atoms with a soft (sp^2 hybridization) carbon framework. They exhibit a high quantum efficiency of 79% with a partially direct bandgap transition, since the atomic distances of the BCNO atoms are smaller than that of BCN compounds. The smaller atomic distances of BCNO are due to the presence of oxygen atoms, which have a high electron affinity and a smaller covalent bond radius compared with boron, carbon and nitrogen. The above results and discussions suggest that the BCNO phosphors are versatile, which shows promise for advanced industry application.

References

- Bai, X.D., E. G. Wang, and J. Yu, "Blue-violet Photoluminescence from large-scale highly aligned boron carbonitride nanofibers", *Appl. Phys. Lett.* 77 (2000) 67-69
- Brydson, R., H. Sauer, W. Engel, J. M. Thomas, E. Zeitler, "EELS as a fingerprint of the chemical co-ordination of light elements", *Microsc. Microanal. Microstruct.*, 2 (1991) 159-169
- Chen, Y. Chen, J. C. Barnard, R. E. Palmer, M. O. Watanabe, and T. Sasaki, "Indirect band gap of light-emitting BC₂N", *Phys. Rev. Lett.*, 83 (1999) 2406.
- Garvie, L. A. J. , H. Hubert, P. Rez, P. F. McMillan, and P. R. Buseck, "BC_{0.5}O_{0.4}C_{0.1}: Carbon- and oxygen-substituted hexagonal BN", *J. Alloys Compd.*, 290 (1999) 34-40
- Guo, Q., Y. Xie, C. Yi, L. Zhu, and P. Gao, "Synthesis of ultraviolet luminescent turbostratic boron nitride powders via a novel low-temperature, low-cost, and high-yield chemical route", *J. Solid. State. Chem.*, 178 (2005) 1925-1928
- Hubert, H., L. A. J. Garvie, P. R. Buseck, W. T. Petruskey, and P. F. McMillan, "High-pressure, high-temperature syntheses in the B-C-N-O system I. Preparation and characterization", *J. Solid State Chem.*, 133 (1997) 356-364
- Kaihatsu, Y, F. Iskandar, H. Widiyandari, W-N. Wang, and K. Okuyama, "Fabrication and characterization of a yellow-emitting BCNO phosphor for white light-emitting diodes", *Electrochemical and Solid-State Letters*, 12 (2009) J33-J36
- Kawaguchi, M., "B/C/N materials based on the graphite network", *Adv. Mater.*, 9 (1997) 615-626
- Keast, V. J., A. J. Scott, R. Brydson, D. B. Williams, and J. Bruley, "Electron energy-loss near-edge structure – a tool for the investigation of electronic structure on the nanometer scale", *J. Microscopy*, 203 (2001) 135.-175
- McMurry, J. and R. C. Fay, *Chemistry*, 3rd Edition, Prentice-Hall, Inc., Upper Saddle River, New Jersey, 2001.
- Nara, S., and S. Ibuki, *Fundamentals of Luminescence*, in *Phosphor Handbook*, 2nd Edition, Taylor & Francis, 2006.
- Neamen, D.A., *Semiconductor Physics and Devices: Basic Principles*, 3rd Edition,

McGraw-Hill, New York, 2003.

Ogi, T., Y. Kaihatsu, F. Iskandar, W-N. Wang and K. Okuyama, "Facile synthesis of new full-color-emitting BCNO phosphors with high quantum efficiency", *Adv. Mater.*, 20 (2008) 3235-3238

Yang, J., T. Qiu, and C-Y. Shen, "New BCN fibres for strong ultraviolet and visible light luminescence", *Chin. Phys. Lett.*, 23 (2006) 2573-2575

Chapter 5

Summary

5.1 Conclusions

Inorganic phosphors as functional materials, are used for the devices for our daily lives, such as, CRT and fluorescence lamp. Moreover, white LED, LD, and organic and inorganic electroluminescent devices are now available; intensive investigation of phosphors is continuing. The requirements of phosphor materials are high luminescence, high efficiency and desirable emission wavelength. In order to exhibit these properties, phosphor materials may have high crystallinity, uniformity of composition, non-agglomeration, etc. To achieve the above requirements, a spray pyrolysis method is potentially promising, since it is a simple, rapid, and continuous process, low cost, and can be used in the fabrication of diverse materials, including phosphors, with controllable size and compositions.

Moreover, phosphors should have a character of economical and environmental advantages, since rare earth elements are expensive and they have limitation of production area.

In this thesis, solid/dense and porous particles of rare earth doped yttrium oxide ($\text{Y}_2\text{O}_3:\text{Eu}^{3+}$) phosphor particles by using spray pyrolysis, and newly synthesized carbon-based boron oxynitride (BCNO) phosphors by one-step liquid process at relatively moderate conditions are selected as model materials.

Chapter 1 discusses the background, previous research, methods used to investigate photoluminescence (PL) phenomena, current state of the field, and problems associated with inorganic phosphors.

Chapter 2 describes the relationship between photoluminescence and both the particle and crystallite size of $\text{Y}_2\text{O}_3:\text{Eu}^{3+}$ fine particles. The crystallite and particle sizes played different roles in the control of the PL characteristics of the phosphors. The blue-shift of the charge transfer band in the excitation spectra was mostly due to the particle-size effect, because the crystallite boundary of the particles had no effect on the charge transfer. In contrast, the decrease in the crystal symmetry ratio, which is the ratio of the C_2 to C_{3i} sub-lattice populations in the PL emission spectra, was primarily due to the effect of crystallite size, because the amorphous/defect parts were located on the surface of the crystallites/particles.

Chapter 3 demonstrates the effect of porosity on the photoluminescence of $\text{Y}_2\text{O}_3:\text{Eu}^{3+}$ fine particles. The porous particles exhibited greater red-emission rendering properties than that of non-porous particles, based on the CIE chromaticity diagram. The submicrometer particles were prepared by spray pyrolysis using a mixture of an yttrium and europium nitrate solution and colloidal polystyrene latex (PSL) particles as the precursor. The photoluminescence intensity and quantum efficiency exhibited by the porous particles are greater than that of non-porous particles because the porous particles are hollow. Porous particles have unique photophysical properties, such as a 4-nm blue-shift in the charge-transfer and a lower symmetry ratio of 2.7, which were not exhibited by the non-porous particles with a particle size of 757 nm and a crystallite size of approximately 30 nm. The properties of sub-micrometer porous particles were identical to those of non-porous particles, which have reduced particle and crystallite size compared with porous particles.

Chapter 4 presents a detailed chemical analysis and photoluminescence characterization of the BCNO phosphors. The BCNO phosphors were synthesized from precursors of boric acid, urea, and polyethylene glycol (PEG) under relatively moderate conditions, low temperature, and an atmospheric environment. The resulting powder has high external quantum efficiency with a direct band-gap transition. The BCNO phosphors have these properties because the coordinates of the BCNO are less than those of conventional BCN compounds, which have an indirect band-gap transition and low quantum efficiency. The smaller coordinates of the BCNO result from the presence

of oxygen atoms, which have higher electron affinity and smaller covalent-bond radii compared with boron, carbon and nitrogen.

This chapter provides a simple summary of the results that photoluminescence characterization and morphology control of inorganic phosphor particles are useful methods for development of new functional materials.

5.2 Suggestions for Further Investigations

$\text{Y}_2\text{O}_3:\text{Eu}^{3+}$ is used as phosphor for long time, but with spray pyrolysis method, it is added new possibility for next generation luminescent material with porous character for cost saving and high functionality. We need to investigate more detail photoluminescence property to create next luminescent material.

BCNO is a newly synthesized material, which made by easy synthesis procedure and does not include rare earth and any metal elements. To reveal the generation mechanism and to exhibit high efficient PL for all emission wavelengths, further investigation is required.

PL method is a high sensitive and adequate method to investigate phosphors, but time resolved technique has more important role in investigating these mechanisms.

Acknowledgements

First of all, I would like to express my deepest gratitude to Prof. Kikuo Okuyama, who has guided me to fruitful research. I have to express my great thanks to assistant Prof. Wei-Ning Wang for giving me a lot of advices and useful discussions. I am very grateful to assistant Prof. Ferry Iskandar for providing me to advice, discussions and guide to research. In addition, I am very grateful to assistant Prof. Takashi Ogi of Osaka Prefecture University, Dr. W. Widiyastuti, and Mr. Yutaka Kaihatsu for providing me to discussions.

I would like to express my thanks to give me a chance to study in graduate school to Horiba Ltd., Chairman, President and CEO, Mr. Atsushi Horiba, and Executive Vice President Dr. Kozo Ishida, and corporate officer Mr. Kenichi Obori, and my colleague Dr. Tetsuji Yamaguchi.

Finally, I would like to thank my family for supporting me to encourage continuing research activities for a long period.

Takaaki MINAMI

Appendix I

List of Figures

Fig.1.1		
Absorption and photoluminescent mechanism. (a) atom, and (b) molecule		6
Fig.1.2		
Relation between (a) absorption and photoluminescence spectra, and (b) energy diagram of ground and excited bands		7
Fig.1.3		
Schematic presentation of energy diagram of species M		9
Fig.1.4		
Photoluminescent decay curves of tetra phenyl porphyrin particles on a glass slide (a) observation using the streak camera method (b) observation using the TC-SPC method		11
Fig.1.5		
Schematic diagram of $Y_2O_3:Eu^{3+}$ lattice and its sub-lattices		16
Fig.1.6		
Schematic diagram of the experimental setup and procedures		19
Fig.1.7		
Schematic representation of (a) photoluminescent (radiation) and (b) non-radiation mechanisms		23
Fig.1.8		
Schematic representation of Graphite, BC_xN_y , and h-BN photophysical characters and their structures.		27

Fig. 1.9	
SEM images of (a) non-porous and (b) porous particles.	30
Fig. 1.10	
Structure of chapters of present thesis	31
Fig. 2.1	
XRD patterns (left) and FE-SEM images (right) of $Y_2O_3:Eu^{3+}$ particles prepared from 0.1 M precursor at (a) 800°C, (b) 1000°C, (c) 1200°C, and (d) 1400°C. The average particle sizes (D_p) are nearly constant at around 900 nm.	42
Fig. 2.2	
XRD patterns (left) and FE-SEM images (right) of $Y_2O_3:Eu^{3+}$ particles prepared from precursors with different concentrations (a) 0.20 M, (b) 0.10 M, (c) 0.05 M, and (d) 0.01 M at 1400°C. The average crystallite sizes (D_c) are nearly constant at around 35 nm	43
Fig. 2.3	
Excitation spectra of $Y_2O_3:Eu^{3+}$ particles with (a) different crystallite sizes and (b) different particle sizes	45
Fig. 2.4	
The excitation wavelength as a function of (a) crystallite size and (b) particle size of $Y_2O_3:Eu^{3+}$ particles	47
Fig. 2.5	
Emission spectra of $Y_2O_3:Eu^{3+}$ particles with (a) different crystallite sizes and (b) different particle sizes, respectively	49
Fig. 2.6	
The symmetry ratio of C_2 (at 587.7nm) to C_{31} (at 582.4nm) as a function of (a) crystallite size and (b) particle size of $Y_2O_3:Eu^{3+}$ particles	51

Fig. 3.1	
FE-SEM images of particles prepared from precursors with PSL contents of (a) 0, (b) 40, (c) 60, and (d) 80 vol%	60
Fig. 3.2	
FE-SEM images of particles prepared from precursors with different concentrations of 80 vol% PSL (a) 0.0376, (b) 0.1 and (c) 0.15 M	61
Fig. 3.3	
XRD patterns of particles with different porosities and particle sizes	63
Fig. 3.4	
PL emission spectra of $Y_2O_3:Eu^{3+}$ particles as functions of (a) porosity plotted against volume percentages of added PSL and (b) particle size with a constant PSL content of 80 vol%; and (c) magnified PL spectra from 570 to 600 nm for both porous (80 vol%) and non-porous particles	65
Fig. 3.5	
PL excitation spectra of $Y_2O_3:Eu^{3+}$ particles as a functions of (a) porosity and (b) particle size	67
Fig. 3.6	
Relative PL emission peak intensity and crystallite size of the generated particles as functions of (a) porosity and (b) particle size	69
Fig. 3.7	
CIE chromaticity diagram of $Y_2O_3:Eu^{3+}$ particles with different porosities and particles sizes (samples of Y-1 to Y-7) as indicated in Table 3.1	71

Fig. 4.1

Representative electron energy loss spectra of BCNO phosphors prepared at 800 °C for 30 min with PEG/B = 2×10^{-3} (mol/mol). (a) total spectrum, (b) ionization edges of Boron, (c) ionization edges of Carbon, (d) ionization edges of Nitrogen, and (e) ionization edges of Oxygen.

79

Fig. 4.2

Relative energy loss spectra of K edges of BCNO phosphor. All spectra on a common energy scale and shifted to align relative to their signal of Electron energy loss spectroscopy. Dotted line is indicating relative energy loss of 2 and 10 eV

80

Fig. 4.3

Photoluminescence spectra of phosphor particles with different sample preparation. (a) PL spectrum of phosphor particles and (b) PL Peak wavelength (circle) and its quantum efficiency (triangle) of phosphor particles, prepared by processing temperature at 700, 800 and 900 °C for 30 min and prepared using PEG/B = 2.0×10^{-3} (mol/mol)

83

Fig. 4.4

Photoluminescence spectra of phosphor particles with different sample preparation. (a) PL spectrum of phosphor particles and (b) PL Peak wavelength (circle) and its quantum efficiency (triangle) of phosphor particles, prepared by heating time at 30, 45, and 60 min for 700 °C, and prepared using PEG/B = 4.0×10^{-3} (mol/mol) for 60 min and 45 min, PEG/B = 4.4×10^{-3} (mol/mol) for 30 min.

84

Appendix II

List of Tables

Table 1.1	
Luminescent Phenomena	3
Table 1.2	
Photoluminescence lifetimes of various materials in liquid ($1 \times 10^{-5} \text{M}$) measured using a streak camera and the TC-SPC technique	10
Table 1.3	
Photoluminescence lifetimes of TPP deposit	12
Table 1.4	
Luminescence Phenomena and Inorganic Phosphor	15
Table 1.5	
Position of the Eu^{3+} charge-transfer band of the ${}^5\text{D}_0 \rightarrow {}^7\text{F}_j$ photoluminescence after excitation in the charge transfer band	26
Table.1.6	
Photoluminescence wavelengths of BN/BCN	28
Table 3.1	
Effect of porosity and particle sizes on crystallite size, QE and CIE coordinates.	59

Appendix III

List of Publications

Chapter 1

Minami, T., and S. Hirayama, “High quality fluorescence decay curves and lifetime imaging using an elliptical scan streak camera”, J. Photochem. Photobio A: Chemistry, 53 (1990) 11-21

Chapter 2

Minami, T., W-N. Wang, F. Iskandar, and K. Okuyama, “Photoluminescence properties of submicrometer phosphors with different crystallite/particle sizes”, Jpn. J. Appl. Phys.: 47 (2008) 7220-7223

Chapter 3

Widiyastuti, W., T. Minami, W-N. Wang, F. Iskandar, and K. Okuyama, “Photoluminescence Characteristics of Ordered Macroporous Eu-doped Yttrium Oxide Particles Prepared by Spray Pyrolysis”, Jpn. J. Appl. Phys. in press

Chapter 4

Minami, T., W-N. Wang, Y. Kaihatsu, F. Iskandar, and K. Okuyama, “Photoluminescence and Electron Energy Loss Spectra Analysis of New Carbon-based Boron Oxynitride Phosphor Particles”, J.Mater.Sci. in review